The 'zoo' of secondary instabilities precursory to stratified shear flow transition. Part 1 Shear aligned convection, pairing, and braid instabilities

A. Mashayek† and W. R. Peltier

Department of Physics, University of Toronto, Ontario, M5S 1A7, Canada

We study the competition between various secondary instabilities that co-exist in a preturbulent stratified parallel flow subject to Kelvin–Helmholtz instability. In particular, we investigate whether a secondary braid instability might emerge prior to the overturning of the statically unstable regions that develop in the cores of the primary Kelvin–Helmholtz billows. We identify two groups of instabilities on the braid. One group is a shear instability which extracts its energy from the background shear and is suppressed by the straining contribution of the background flow. The other group, which seems to have no precedent in the literature, includes phase-locked modes which grow at the stagnation point on the braid and are almost entirely driven by the straining contributions of the background flow. For the latter group, the braid shear has a negative influence on the growth rate. Our analysis demonstrates that the probability of finite-amplitude growth of both braid instabilities is enhanced with increasing Reynolds number and Richardson number. We also show that the possibility of emergence of braid instabilities decreases with the Prandtl number for the shear modes and increases for the stagnation point instabilities. Through detailed non-separable linear stability analysis, we show that both braid instabilities are fundamentally three dimensional with the shear modes being of small wavenumbers and the stagnation point modes dominating at large wavenumber.

Key words: shear layer turbulence, stratified turbulencence, transition to turbulence

---

1. Introduction

In both stratified and unstratified shear flows, the transition to turbulence is known to occur through a finite sequence of steps in accord with the qualitative theory of Ruelle & Takens (1971). In either case the first step in this sequence usually involves the growth to finite amplitude of an inherently two-dimensional primary instability (for a counterexample, see Smyth & Peltier (1990)), of which Kelvin–Helmholtz (KH) billows (Kelvin 1871) are the canonical example.

KH waves have been ubiquitously observed and studied in the atmospheric context (Ludlam 1967; Browning & Watkins 1970; Browning 1971; Gossard 1990; and more recently by Luce 2010). In the oceans, KH waves have been found near the surface

† Email address for correspondence: amashaye@atmosp.physics.utoronto.ca

(Woods 1968; Thorpe 1978; Haury, Briscoe & Orr 1979; Marmorino 1987), in the deep ocean induced by large-scale internal wave shear (Haren & Gostiaux 2010), in an energetic estuarine shear zone (Geyer *et al.* 2010) and accompanying internal solitary waves propagating shoreward over the continental shelf (Moum *et al.* 2003; Lamb & Farmer 2011). Although most of the oceanic observations reveal very few KH billows, the studies by Geyer *et al.* (2010) and Haren & Gostiaux (2010) provide evidence of a train of KH billows similar to those often observed in the atmosphere and in laboratory experiments (Thorpe 1971, 1981, 1987; Holt 1988; Caulfield, Yoshida & Peltier 1996; or see Thorpe 2005 for a thorough review). Owing to experimental limitations, the parameter space in which the experiments are performed is most often far from appropriate to either of the natural systems. Even though both laboratory and *in situ* ocean/atmosphere observations reveal the emergence of a primary KH wave, the large difference in the governing Reynolds and Prandtl numbers may lead to significant differences in the second step in the route to turbulent collapse and the attendant enhanced molecular dissipation and irreversible mixing.

In this study, the focus will be upon stratified shear layers as opposed to those of constant density. Although KH instability arises in both circumstances (Smyth & Peltier 1994; Potylitsin & Peltier 1998), the subsequent dynamics differ considerably due to the influence of the stratification. In stratified shear flows, the buoyancy force gives rise to a plethora of secondary instabilities which provide mechanisms through which the primary KH billows may undergo turbulent collapse. Over the past several decades, the majority of the theoretical and numerical research in this field has been focused upon such secondary instabilities of the primary KH waves (Corcos & Sherman 1976; Klaassen & Peltier 1985, 1989, 1991; Smyth & Peltier 1990, 1991, 1993, 1994; Caulfield & Peltier 1994; Staquet 1995; Cortesi, Yadigaroglu & Bannerjee 1998; Caulfield & Peltier 2000; Staquet 2000; Smyth, Moum & Caldwell 2001; Smyth 2003).

Once an array of primary KH vortices develop in a mixing layer, the vortices are known to be susceptible to several secondary instabilities. One of these instabilities is the amalgamation instability (Klaassen & Peltier 1989) (hereafter referred to as *KP89*) which in its most common form corresponds to vortex pairing (Winant & Browand 1974; Pierrehumbert & Widnall 1982; *KP89*). Theoretical analysis of *KP89* demonstrated that the pairing instability has a sufficiently high growth rate that it should inevitably be realized in the regime of modest Reynolds number characteristic of laboratory circumstances. It remains a significant issue as to whether this interaction may also occur in the higher-Reynolds-number regime that is characteristic of oceanographic and atmospheric circumstances. Indeed, merging events have seldom been observed in these natural systems. One of our goals is to understand whether there might exist physical processes at high Reynolds numbers which would precede and thereby inhibit the pairing interaction. One of the best studied of such three-dimensional instabilities is the shear-aligned convective instability (which arises due to overturning of statically unstable regions inside the vortex cores) first predicted by Davis & Peltier (1979), and thereafter studied in detail by Klaassen & Peltier (1985) (hereafter referred to as *KP85*) and Caulfield & Peltier (1994) Caulfield & Peltier (2000) (hereafter referred to as *CP00*). Experimental studies of Thorpe (1987) and Caulfield *et al.* (1996) also clearly revealed the occurrence of this secondary instability and its important role in the transition of the flow to turbulence in the regime of moderate Reynolds number. Another well-known secondary instability is the secondary shear instability of the vorticity braid (the vorticity filament which connects adjacent vortex cores in a train of billows) first predicted by Corcos & Sherman (1976) (hereafter referred to as *CS76*) and further studied in Staquet (1995, 2000)

and Smyth (2003) (hereafter referred to as *S03*). Evidence of such secondary braid vortices has been reported by Geyer *et al.* (2010) and perhaps also by Thorpe (1978) (figure 2*b* of the latter seems to show braid vortices). A third group of instabilities which grow on the braid of a KH instability in a stratified layer, and which have previously been spotted but not properly discussed in terms of their origin, will be discussed in this work. This group of instability modes primarily extract their energy from the background strain field. Dritschel *et al.* (1991) discussed this group in the context of an infinitely long vorticity layer in an unstratified environment. We will show how these modes become relevant in the context of this work.

The above-referenced analyses of the braid instability have suggested that this instability may play a major roll in turbulence transition. As the secondary convective instability (which is not realizable in two-dimensional simulations) provides a rapid route to turbulence (*CP00*), it remains an important question as to whether the previously referenced two-dimensional numerical simulations showing emergence of braid shear instabilities are at all relevant to the understanding of a three-dimensional flow. In the present paper we address this question by performing detailed non-separable linear stability analyses of the primary train of KH billows. Our main goal is to study the competition between the pairing, shear aligned convection and braid shear instabilities. Our approach will employ the methodology of *KP85*.

As the secondary linear stability analysis consumes a lot of numerical resources, in the first half of this paper we develop a simple physics-based model (based on *CS76* and *S03* for braid instability and *KP85* for secondary convective instability) to predict maps of susceptibility for the braid shear and core convective instabilities. In the remainder of this paper (as well as in the companion paper Mashayek & Peltier (2012), hereafter referred to as *MP2*), these maps are employed as a guide in choosing the regions of parameter space in which detailed non-separable instability analysis is performed. In *MP2* we provide a detailed investigation of the effect of stratification on the set of secondary instabilities to which a KH billow may be subject and of the energetics of the secondary modes and their influence upon irreversible mixing.

We will repeatedly refer to several secondary instabilities in this paper and in *MP2* by referring to their acronyms. This may make it difficult for the reader to remember what each acronym represents. Therefore, a secondary instability lexicon is provided in figure 19 in the Appendix. Also, to avoid confusion, reference to previous contributions to the literature will also appear in the form of acronyms but these will appear in italics (such as *MP2*, *CS76* etc.) while instability acronyms will not. The appendix also includes a table which can be used to remind the reader of which studies the italicized acronyms refer to.

2. Theoretical preliminaries: formulation of the problem and numerical solution of the governing equations

We consider a stably stratified shear layer which is horizontally periodic in space and evolves with time. The flow domain is described in Cartesian coordinates with x and z denoting the streamwise and vertical directions, respectively. The initial background profiles of velocity and density are assumed to be of the form

$$\bar{U}^{\star}(z^{\star}) = U_0 \tanh\left(\frac{z^{\star}}{h}\right), \tag{2.1}$$

$$\bar{\rho}^{\star}(z^{\star}) = \rho_a - \rho_0 \tanh\left(\frac{Rz^{\star}}{h}\right), \tag{2.2}$$

where U_0 and ρ_0 are reference velocity and density, h is half the shear layer thickness, and R is the ratio of the characteristic scale of velocity variation to that of the density variation and is chosen to be 1.1 based on some experimental observations (Thorpe 1985, 1987; Caulfield *et al.* 1996) in which the working fluid is salt stratified water. It should be noted that this value can be larger, however, we keep it constant to avoid further complicating an already complex parameter space to be explored in this paper. A flow configuration such as this is known to be most unstable to two-dimensional KH instability (see Drazin & Reid 1981) provided that the gradient Richardson number defined by

$$Ri(z^\star) = N^2/(\text{shear})^2 = \frac{-g}{\rho_0}\frac{\partial\rho^\star}{\partial z^\star} \bigg/ \left(\frac{\mathrm{d}\bar{U}^\star}{\mathrm{d}z^\star}\right)^2 \qquad (2.3)$$

is sufficiently small. Based upon the theorem of Howard (1961) and Miles (1961), it is well understood that a necessary condition for instability is that the Richardon number achieves a value less than $1/4$ somewhere in the flow. Under this condition, the destabilizing influence of the velocity shear is sufficient to overcome the stabilizing influence of the density stratification. It is the onset of the primary KH instability that provides the necessary background for growth of secondary instability(s) which eventually lead to turbulent collapse of the mixing layer.

For the profiles described by (2.1) and (2.2), the gradient Richardson number at the centre of the shear layer, Ri_0, has the lowest value in the initial profiles and therefore we regard it as the appropriate measure of the stratification within the flow. Our non-dimensionalization of the governing equations is based upon the following choices for the scales of time, distance, velocity, pressure and density, respectively:

$$t = t^\star U_0/h, \quad x_i = x_i^\star/h, \quad u_i = u_i^\star/U_0, \quad p = p^\star/\rho_0 U_0^2, \quad \rho = \rho^\star/\rho_0 \qquad (2.4)$$

where $\rho^\star$ and $p^\star$ are departures from hydrostatic balance. We also assume that the flows are incompressible with density variations small enough for the Boussinesq approximation to be valid. The equations of motion, incompressibility and continuity in dimensionless form then reduce to

$$\frac{\mathrm{D}u_i}{\mathrm{D}t} = -\frac{\partial p}{\partial x_i} - \frac{Ri_0}{R}\rho\delta_{i2} + \frac{1}{Re}\frac{\partial^2 u_i}{\partial x_j^2}, \qquad (2.5)$$

$$\frac{\partial u_i}{\partial x_i} = 0, \qquad (2.6)$$

$$\frac{\mathrm{D}\rho}{\mathrm{D}t} = \frac{1}{Re\, Pr}\frac{\partial^2 \rho}{\partial x_j^2}, \qquad (2.7)$$

where $(i, j = 1, 2)$ for the fully nonlinear but two-dimensional flows for which these governing equations will be numerically integrated to produce the basic states whose stability we will investigate to three-dimensional perturbations. The Reynolds number is defined by $Re = U_0 d/\nu$ where ν is the kinematic viscosity and the Prandtl number by $Pr = \nu/\kappa$ where κ is the thermal diffusivity.

Throughout this study, we will primarily consider flows in the range $1000 < Re < 2000$, $0.04 < Ri_0 < 0.2$ and $1 < Pr < 4$. Equations (2.5)–(2.7) provide the starting point from which our theoretical analyses will follow. The numerical methods we employ are constructed to provide fully resolved direct numerical simulations (DNSs) of those equations. The algorithm we employ is that described in detail by Taylor (2007) and Bewley (2011). Periodic boundary conditions are applied in the streamwise direction with derivatives in this direction being treated using a pseudo-spectral

method. The derivatives in the vertical direction are computed using second-order finite differences. The numerical scheme ensures the discrete conservation of mass, momentum and energy. To allow for the growth of the pairing instability in the flow, the horizontal extent of the domain is chosen to be twice the wavelength of the most unstable KH mode (based on inviscid linear theory) of the background velocity and density profiles. Calculations similar to those of Hazel (1972) led to $\lambda = 14.27h$, implying a horizontal domain scale of $28.54h$ (for two wavelengths) for the case in which the Richardson number is 0.04. The vertical extent of the computational domain has been chosen to be 30 times the half-shear-layer depth, h. This is sufficiently large to ensure that the flow remains unaffected by the horizontal boundaries even in cases in which pairing occurs. Resolution studies have been conducted to ensure that all of the simulations are fully resolved. A solid test of accuracy of the simulations is to investigate whether equation (2.20) of *CP00* holds true during flow evolution. A list of all two-dimensional numerical simulations which will be employed to verify the findings of our to-be-discussed heuristic model or to provide the background flow required for non-separable stability analysis is provided in table 1. For all simulations listed in the table, this equation was satisfied to better than one part in 10^6. It is important to note that even though the resolution of our simulations is high enough to resolve all energized scales throughout the life cycle of the two-dimensional KH wave, these simulations will not be used to study the turbulent phase of the flow. This is because two-dimensional simulations become irrelevant to real three-dimensional flows as soon as the necessary environment for growth of three-dimensional instabilities develops. We employ these two-dimensional simulations simply to provide background flows during the laminar phase of KH wave evolution to serve as basic states for the purpose of our secondary stability analyses.

The required two-dimensional simulations are initialized by the addition of a very small amplitude perturbation in the form of the most unstable KH mode to the velocity and density fields defined by the background profiles (2.1) and (2.2) to stimulate the growth of primary KH instability and save computational resources. To ensure that this initialization does not have any significant impact on the results, the amplitude of this initial disturbance is chosen to be extremely small with its corresponding kinetic energy being 10^{-5} times that of the background shear flow enclosed within a distance of $5h$ from the centre of the shear layer. To allow for an unbiased initiation of any secondary instability to which the flow may be prone, we also add incompressible white noise to the velocity field and white noise with zero mean to the density field. The non-dimensional amplitudes the primary KH wave and the white noise are 10^{-2} and 10^{-4}, respectively. Free-slip impermeable boundary conditions on velocity components are applied at the top and bottom boundaries of the domain, together with a condition of zero density flux.

3. Physical models for the shear aligned convective and braid instabilities

In this section we develop simple models capable of predicting the time variations in the strength of the secondary shear instability (SSI) of the braid and secondary convective instability (SCI) of the core. The model for the latter is based upon the Rayleigh number of the unstable regions (Ra^u) that form in the cores of the KH billows as the density field is rolled up by the growth of the wave as discussed in *KP85*. In the latter case we employ theoretical analyses of *CS76* to estimate the minimum Richardson number in the braid of the KH wave after it has grown to its maximum amplitude. Together, these heuristic analyses will enable us to propose a

Case name	Grid $(Nx \times Nz)$	t_m	t_{md}	$\Delta^u_{\rho m}$	δ^u_m	δ^u_{md}	H_m (*CS76*)	t_m (*CS76*)
c1-1000-0.04	768 × 800	45	51	1.91	0.75	0.64	3.34	56
c1-1000-0.08	768 × 800	55	57	1.73	0.65	0.58	2.9	61
c1-1000-0.12	768 × 800	66	66	1.37	0.45	0.45	2.54	65
c1-1000-0.16	768 × 800	81	78	0.83	0.39	0.41	2.22	73
c1-1000-0.20	768 × 800	130	109	0.21	0.25	0.33	1.94	85
c1-2000-0.04	768 × 800	42	51	2.0	0.65	0.55	3.34	56
c1-2000-0.08	768 × 800	55	55	1.95	0.5	0.5	2.9	61
c1-2000-0.12	768 × 800	64	66	1.74	0.48	0.45	2.54	65
c1-2000-0.16	768 × 800	77	77	1.2	0.4	0.4	2.22	73
c1-2000-0.20	768 × 800	130	117	0.48	0.26	0.26	1.94	85
c2-1000-0.04	768 × 800	45	52	2	0.6	0.45	3.34	56
c2-1000-0.08	768 × 800	54	58	1.96	0.55	0.46	2.9	61
c2-1000-0.12	768 × 800	67	65	1.65	0.45	0.49	2.54	65
c2-1000-0.16	768 × 800	85	81	0.94	0.34	0.38	2.22	73
c2-1000-0.20	768 × 800	116	97	0.15	0.26	0.26	1.94	85
c2-2000-0.04	768 × 800	44	52	2	0.5	0.45	3.34	56
c2-2000-0.08	768 × 800	55	61	1.96	0.37	0.37	2.9	61
c2-2000-0.12	768 × 800	66	66	1.98	0.45	0.45	2.54	65
c2-2000-0.16	768 × 800	83	80	1.38	0.37	0.4	2.22	73
c2-2000-0.20	768 × 800	127	110	0.38	0.23	0.19	1.94	85
c4-1000-0.04	2048 × 2208	45	55	2	0.5	0.38	3.34	56
c4-1000-0.08	2048 × 2208	55	60	2	0.44	0.41	2.9	61
c4-1000-0.12	2048 × 2208	68	66	1.9	0.35	0.37	2.54	65
c4-1000-0.16	2048 × 2208	83	82	1.1	0.31	0.31	2.22	73
c4-1000-0.20	2048 × 2208	125	88	0.15	0.26	0.26	1.94	85
c4-2000-0.04	2048 × 2208	44	52	2	0.45	0.3	3.34	56
c4-2000-0.08	2048 × 2208	54	61	2	0.37	0.34	2.9	61
c4-2000-0.12	2048 × 2208	66	69	2	0.29	0.27	2.54	65
c4-2000-0.16	2048 × 2208	83	80	1.3	0.31	0.32	2.22	73
c4-2000-0.20	2048 × 2208	115	90	0.29	0.24	0.18	1.94	85

TABLE 1. Two-dimensional numerical simulations performed to provide the basis for the non-separable secondary stability analyses discussed in this paper and in the companion paper *MP2* and also used for verification of the theoretical model discussed in § 3. Parameters representing each column of the table will be defined in subsequent sections.

map which will help in predicting the probability of occurrence of the two instabilities in various regions of the three-dimensional *Pr–Re–Ri* parameter space.

Table 1 provides the details of the two-dimensional simulations to be employed in what follows. All test cases are labelled as '*case Pr–Re–Ri*'. For example, c1-1000-0.04 refers to a case with $Pr = 1$, $Re = 1000$ and $Ri_0 = 0.04$. To avoid confusion with the acronyms used for secondary instabilities, as stated previously we will employ italic notation for references to previous work (such as *CS76*). We will also use the prefix '*SM−*' for reference to the materials in the supplementary material (available at journals.cambridge.org/flm).

3.1. *A heuristic model for the baroclinic vortex core*

As the amplitude of the KH wave increases and the billow 'rolls up', unstable regions of relatively heavy fluid become superimposed over regions of light fluid within the billow cores (see figure 1*a–d*). It was speculated by Davis & Peltier (1979) and then shown by *KP85* that these unstable regions achieve sufficiently large Rayleigh
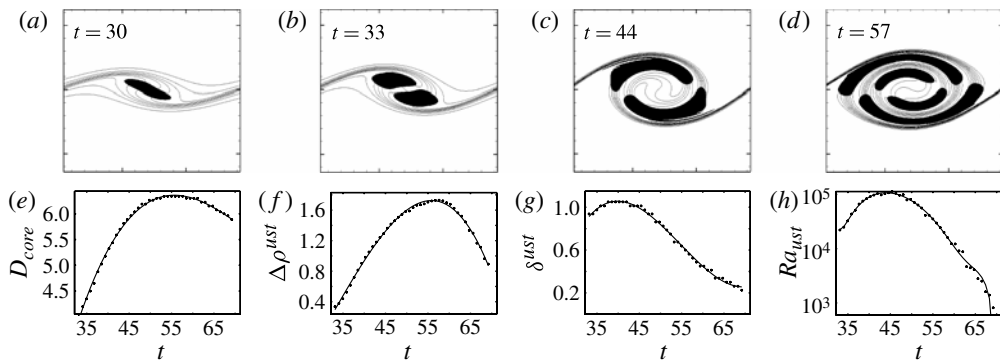
FIGURE 1. Density contours overlaid by shaded unstable regions for $t = 30, 33, 44, 57$ shown in (*a*) through (*d*). Evolution of: (*e*) diameter of the core; (*f*) $\Delta\rho^u$; (*g*) δ^u; and (*h*) Ra^u. All the plots are from a case with $Re = 1000$, $Pr = 1$ and $Ri_0 = 0.08$. '+' indicates actual points extracted from the simulation and lines are simple polynominal fits to them.

numbers, even at modest Reynolds numbers, to support SCI. It was later established by Caulfield & Peltier (1994) and *CP00* that the shear aligned convective instability arises in three-dimensional DNS analyses of such flows and is responsible for turbulent transition. In this section we develop a qualitative model of the SCI to predict how the possibility of its realization should vary with Reynolds, Prandtl and Richardson numbers.

Figure 1 shows the appearance and time evolution of various unstable regions inside the cores for a test case. In general, a new unstable region forms after each complete overturning of the core. We choose to monitor the Rayleigh number of the outermost unstable region (which has the largest Rayleigh number, Ra^u) as a measure of the susceptibility of the flow to onset of the SCI. We intend to estimate Ra^u at times up to and beyond the point of maximum amplitude of the KH wave. The Rayleigh number of the primary unstable region is defined as

$$Ra^u = Re^2 Pr Ri_0 \frac{\Delta\rho^u}{\Delta\rho_0} \left(\frac{\delta^u}{h} \right)^3 \tag{3.1}$$

where $\Delta\rho^u$ is the density difference across the primary (or outermost) unstable region, $\Delta\rho_0$ is half the density difference across the original shear layer (which has a value of unity in non-dimensional units) and δ^u is the thickness of the primary unstable region. As shown in figure 1, δ^u decreases with time as the number of unstable regions increases and so does $\Delta\rho^u$ due to diffusion. So, after Ra^u reaches a maximum at a time close to the time of maximum billow amplitude (t_m), it thereafter decreases (figure 1*h*). The value of Ra^u at t_m is supercritical for flows with a sufficiently large Reynolds number and the main question is whether Ra^u remains supercritical for long enough to allow for the SCI to fully develop.

To extract the required information from the DNS calculations for calculating Ra^u, we extract (for each time step) a profile through the centres of the cores and measure the core thickness D_{core} and the time evolution of $\Delta\rho^u$ and δ^u. Figure 1(*e–g*) shows the results for D_{core}, $\Delta\rho^u$ and δ^u for the test case. The core reaches its maximum amplitude at time $t_m = 55$ which is very near the time at which $\Delta\rho^u$ peaks. However, δ^u reaches its maximum earlier at $t \sim 40$ and by t_m, δ^u is already decreasing. Figure 1(*h*) shows Ra^u calculated using the information extracted from the simulation.

The value of Ra^u falls below 10^3 near $t = 70$ and the probability of SCI emergence diminishes rapidly beyond this point. By assuming that Ra^u can be meaningfully employed as a measure of the susceptibility of the flow to the occurrence of SCI, and also assuming that the critical Rayleigh number for convective instability is of the order of 10^3, panel (*h*) indicates that the possibility of SCI exists over a relatively long period of time during KH billow evolution. Our choice of the nominal value of 10^3 for the critical Reyleigh number is simply motivated by the fact that in heated from below plane-layer convection, the actual critical value ranges from 658 for stress-free boundaries to 1760 for no-slip boundaries. Please note that even though the unstable region is sheared, since the SCI is shear aligned this shear will exert no significant influence upon the critical value for onset.

In order to estimate Ra^u and its time evolution as a function of *Re*, *Pr* and Ri_0, we require estimates of: (i) t_m; (ii) the value of $\Delta \rho^u$ at t_m and beyond; and (iii) the time evolution of δ^u.

3.1.1. *Estimating t_m*

We know that t_m is primarily a function of Ri_0 and relatively independent of *Re* and *Pr* and it is not accurately estimated using the model of *CS76*. We have obtained a third-order polynominal fit to a set of numerical simulations (listed in table 1) for t_m using regression analysis. In our subsequent analysis we will use this fit as representative of t_m as a function of the initial Richardson number, Ri_0.

3.1.2. *Estimating $\Delta \rho_m^u$*

Figure 1(*f*) shows that the density difference across the primary unstable region of the core reaches a maximum value of $\Delta \rho_m^u = 1.73$ which is slightly less than 2, the density difference across the initial shear layer. The deficit is due to the action of molecular diffusion during the roll-up of the KH billow. For cases with $Ri_0 < 0.16$, $\Delta \rho_m^u$ is closer to 2 but it becomes much smaller as $Ri_0 \to 0.2$ (see the fifth column of table 1). This is because the growth of the KH wave is suppressed by the increase in the stratification leading to a larger roll-up time and hence more time for diffusion of density. In our calculations of the Ra^u, we will employ the following linear correlation between $\Delta \rho_m^u$ and t_m (see figure $SM - 2(b)$ in the supplementary material for a more detailed discussion):

$$\Delta \rho_m^u = 3.22 - 0.024 t_m. \qquad (3.2)$$

3.1.3. *Estimating δ^u*

As shown in figure 1, the thickness of the primary unstable region of the core reaches its maximum at some time prior to t_m and then decreases afterwards. As approximately one new unstable layer is formed with each overturn of the core, we take the number of unstable regions to be proportional to the number of overturns, n, where $n \propto t/t^o$ and t^o is the characteristic overturn time equal to λ/U_0. So, we have tU_0/λ (where λ is the wavelength of the primary KH wave). The thickness of the primary unstable region is proportional to the inverse of the number of unstable regions and so we can write $\delta^u(t) \propto \lambda/U_0 t$. A least squares fit to our simulation data for δ^u at t_m leads to a proportionality constant of unity and an exponent of 0.85 for t_m giving (noting that $U_0 = 1$):

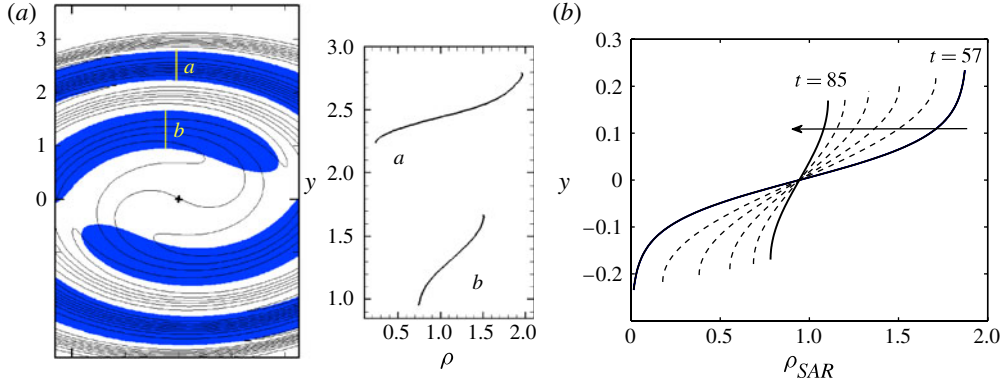$$\delta_m^u = \frac{\lambda}{t_m^{\,0.85}}. \qquad (3.3)$$

FIGURE 2. (Colour online) (*a*) On the left: density contours overlain by the primary and secondary regions (shaded regions) for the case *c*1-1000-0.08 at t_m. On the right: density profiles across the two shown unstable regions at cross-sections *a* and *b*. The origin of the vertical coordinate shown by *y* is the centre of the core marked by a '+'. (*b*) Evolution of the primary unstable region of the case shown in (*a*) obtained by solving a one-dimensional diffusion equation (and not from the simulation). The arrows show increase in time from $t_m = 57$ to $t = 85$.

The deviation of the power of t_m from unity is due to the fact that during the very early stages of KH billow evolution, the number of unstable regions is not yet precisely proportional to the number of overturns.

3.1.4. *Calculation of Ra^u versus time*

We can now estimate the value of the Ra^u at time t_m by using (3.1). Inserting the information for t_m, $\Delta\rho_m^u$ and δ^u into (3.1) leads to

$$Ra_m^u = Re^2 Pr Ri_0 \left(\frac{3.22 - 0.024 t_m}{\Delta\rho_0} \right) \left(\frac{\lambda}{h t_m^{0.85}} \right)^3. \tag{3.4}$$

To calculate the evolution of Ra^u beyond t_m, we need to calculate the time evolution of $\Delta\rho^u$. We note that the density profile across the primary core's unstable regions has a tanh-type profile because it is formed from the roll-up of a tanh-like initial shear layer. Figure 2(*a*) shows the density contours in the core for the case *c*1-1000-0.08 and at time t_m. The density contours are overlain by the primary and secondary unstable regions (shaded regions). The right half of figure 2(*a*) plots the density profiles across each unstable region. The origin of the *y*-axis in the figure is the centre of the core marked by a '+'. The outermost unstable region has a density difference close to two. The density difference across the secondary unstable region is smaller than two and is increasing with time as it moves outward. The thickness of the unstable region also shrinks as it moves outward.

We solve for time evolution of $\Delta\rho^u$ by solving a one-dimensional diffusion equation in the form

$$\frac{\partial\rho}{\partial t} = \frac{1}{Re\,Pr} \frac{\partial\rho^2}{\partial z^2}, \tag{3.5}$$

with the initial condition $\Delta\rho^u = \Delta\rho_m^u$ at t_m and a tanh vertical profile. For simplicity, we neglect the curvature of the primary unstable region since it has already considerably flattened out by t_m. The diffusion equation is solved on a shrinking
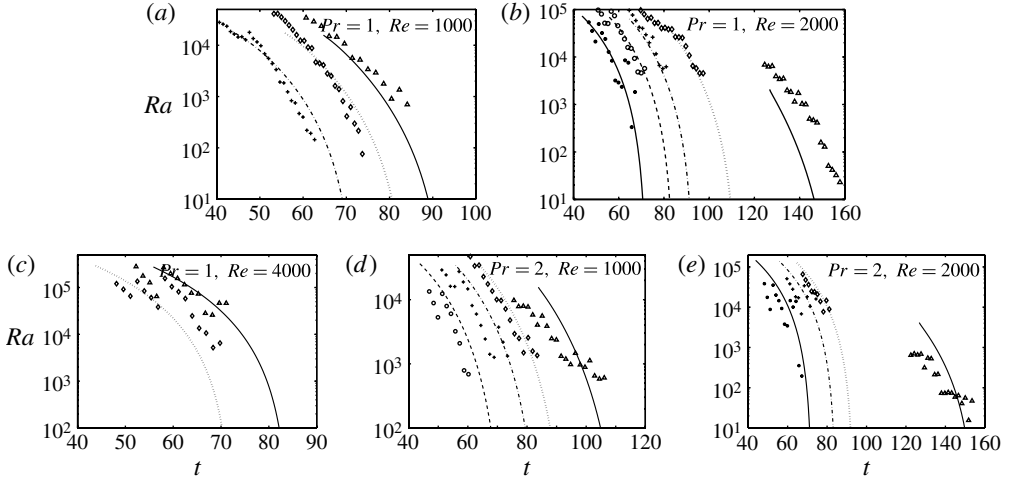
FIGURE 3. Calculations of the Ra^u versus time using the model (lines) plotted alongside data points obtained from the simulations (markers): (*a*) $Pr = 1$, $Re = 1000$; (*b*) $Pr = 1$, $Re = 2000$; (*c*) $Pr = 1$, $Re = 4000$; (*d*) $Pr = 2$, $Re = 1000$; (*e*) $Pr = 2$, $Re = 2000$. The line and marker attributes in each figure are as follows: the solid line with triangles corresponds to $Ri = 0.04$, the dotted line with diamonds corresponds to $Ri = 0.08$, dashed-dotted line with '+' corresponds to $Ri = 0.12$, the dashed line with circles corresponds to $Ri = 0.16$ and the solid thick line with '*' corresponds to $Ri = 0.2$.

grid (according to (3.3)) by using a finite difference discretization, a Crank–Nicolson time stepping method and no density flux boundary conditions at the top and bottom boundaries. Figure 2(*b*) shows the result of the calculation for the primary unstable region shown in frame(*a*). The density difference across the unstable region decreases with time due to diffusion and its thickness decreases as more and more unstable regions form inside the core (see figure 1).

Figure 3 shows the results of the model predictions for time evolution of Ra^u compared with data extracted from the simulations of table 1. The model predictions capture the nature of the decrease in $\Delta\rho_m^u$ fairly accurately. Even though in the construction of the model we employed some information from the simulations, this does not undercut the validity of the model itself and we expect it to be applicable to moderately higher values of the Reynolds and Prandtl numbers for three reasons. First, t_m is mainly a function of Ri_0 alone. Second, $\Delta\rho_m^u$ could be assumed to be two. This would introduce an error which would decrease with increase in Re and Pr. Third, we could assume a unit power for t_m in (3.3).

3.2. *Analysis of the braid*

We begin with the simplified equations proposed in *CS76* which are suggested to govern the evolution of the vorticity and the local shear across the braid:

$$\frac{\partial \Omega}{\partial t} + \frac{\partial}{\partial x'}(u_c \Omega) + \frac{\partial}{\partial z'}(v_c \Omega) = \frac{1}{Re}\frac{\partial^2 \Omega}{\partial z'^2} + Ri_0 \frac{\partial \rho}{\partial z'}\sin(\theta), \tag{3.6}$$

$$\frac{\partial S}{\partial t} + \frac{\partial}{\partial x'}(\bar{U}_B S) = -Ri_0 \Delta\rho \sin(\theta), \tag{3.7}$$

in which $\bar{U}_B = 1/2(u^+ + u^-)$ and u^+, u^- are the braid streamwise velocities at its upper and lower surfaces and S is the shear across the braid. Here x' denotes the streamwise axis of a coordinate system aligned with the braid with its origin located at the stagnation point. Following *CS76*, the along-x'-axis component of the velocity induced by the cores, u_c, is assumed to be directly proportional to the braid downstream displacement through $u_c = \gamma x'$ where γ is the strain rate. As we will see, the braid strain rate plays an important role in our analyses. The strain rate at the stagnation point halfway between two vortex cores in a train of Stuart vortices (Stuart 1967) is given by

$$\gamma_s = -kU\left(\frac{A}{A+1}\right)^{1/2}\left(1 + \frac{A}{A+1}\right)^{1/2} \tag{3.8}$$

where $k = 2\pi/\lambda$ is the wavenumber of the train of vortices and A is a parameter between 0 and 1 that is related to the ratio of the vorticity in the cores (Γ_c) to the total vorticity ($\Gamma = 2\lambda U$) through $A = \tan^2(0.25\pi\Gamma_c/\Gamma)$. The local tilt angle of the braid at this location is given by (*CS76*)

$$\psi = \sin^{-1}\left[\left(\frac{A}{A+1}\right)^{1/2}\right]. \tag{3.9}$$

An important parameter used in analyses by Staquet (1995) and *S03* in studying the SSI of the braid is γ_s/Ω_s. Ω can be calculated by integration in time of (3.6) and Ω_s can be obtained by evaluating Ω at $x' = 0$.

We closely follow the procedure of *CS76* and calculate the evolution of the flow associated with the braid. Both the braid strain rate and tilt angle will be needed once we employ the model of *S03* to calculate the braid Richardson number. In the supplementary material we provide a sample *CS76* calculation and point out how these parameters vary with time during flow evolution. Comparison between the predictions of *CS76* and our two-dimensional numerical simulation results demonstrate that the *CS76* model provides good estimates for the evolution of the braid tilt angle (although the agreement diminishes for $Ri_0 > 0.16$, see the supplementary material for details) but does not accurately predict the time scale of evolution of the basic KH wave. This is because the final stage of evolution in the model calculation is assumed to occur when all of the vorticity in the braid has been transported into the cores. This process is not especially sensitive to the flow field which advects the vorticity. Therefore, using Stuart vortices to represent the flow field of KH billows leads to acceptably accurate results. However, the time required for the transport depends directly on the flow field and so using Stuart vortices leads to an incorrect estimation of the time of evolution. This can be seen by comparing the third column of table 1 (which is labelled t_m and includes the time at which the KH waves reach their maximum amplitude in the simulations) with the last column (which contains the same time calculated based on the *CS76* method).

In the literature Ri_B has been used as one measure of the susceptibility of the braid to SSI. *S03* (following the approach of *CS76*) proposed relations for Ri_B by considering the braid to be an infinitely long tilted shear filament. As pointed out by Dritschel *et al.* (1991) and also noted by Staquet (1995) and *S03*, the strain field induced by the cores can decrease the possibility of SSI significantly. Our two-dimensional simulations also support this. We verify the findings of Dritschel *et al.* (1991) and Staquet (1995) regarding the influence of the core-induced strain field on

the braid using non-separable stability analyses in following sections. As we will also see, however, these findings will need to be significantly extended.

The following relation for Ri_B was proposed in *S03* based on the equilibrium similarity theory of *CS76* (noting that this equation corresponds to an infinitely long braid; in the case of a KH wave, the most relevant point on the braid is the stagnation point, therefore we use γ_s instead of γ in this equation):

$$Ri_B = \frac{(2\pi)^{1/2}\,\gamma_s^{3/2}Pr^{3/2-\beta}}{Re^{1/2}Ri_0\Delta\rho_b\sin(\psi)\tan(\psi)},\tag{3.10}$$

where $\Delta\rho_b$ is the density difference across the braid (usually close to two) and $\beta = 0.6307$ for $1 < Pr < 7$. The velocity and density gradients used in the definition of the braid Richardson number are defined with respect to the proper braid coordinate system (x'–z'). The equilibrium similarity analysis of *S03* can be applied to the flow either prior to or after adjacent cores have merged as the analysis does not rely on the details of the core interior. The simulations described in *S03* were initialized in such a way that the pairing process occurred soon after the KH wave had reached its maximum amplitude. Under these circumstances it was shown that secondary shear instabilities emerged on the braid after the two cores had merged rather than at an earlier stage prior to the merging event. Had the flow initialization employed in *S03* not favoured the pairing process, merging would have occurred at a later time providing more time for secondary instabilities (such as SCI or braid SSI) to grow as shown in Staquet (1995) for SSI. In agreement with Staquet (1995), our two-dimensional simulations show that even with white noise initialization a SSI of the braid is not guaranteed prior to pairing for small Ri_B (due to the influence of the strain field) but it might be possible afterwards (with almost the same Ri_B). As *S03* employed (3.10) in his analysis only to post-pairing braids, we have verified that it is also applicable to pre-pairing braids by comparing its predictions with those of our two-dimensional simulations (see table SM1 in the supplementary material for details).

In order to extract braid information from the simulations, we have developed appropriate diagnostic tools, details of which are discussed in the supplementary material along with their application to case c1-2000-0.12. We will employ this toolbox in the analyses to follow in the remainder of this paper as well as in the companion paper *MP2*.

3.3. *A secondary instability phase diagram*

Figure 4(*a*) shows plots of variations in Ra^u for times beyond t_m (the 't-axis' is shifted by an amount t_m). The data reveals a clear increase in Ra^u with an increase in Pr for fixed values of Ri_0 and Re. This is because an increase in Pr implies a slower diffusion of the unstable regions inside the core and hence a larger density difference across the region which translates into larger Ra^u. Figure 4(*b*) in the figure shows the change in Ra^u with an increase in Re at fixed Pr and Ri_0. An increase in Re also increases the probability of the secondary convective instability by increasing the value of Ra^u. This can be interpreted in two ways. If the increase in Re is achieved through an increase in the shear layer velocity at a fixed value of ν, it leads to an increase in the relative strength of the vorticity bands that develop within the core during the roll-up process. This suppresses diffusion across the vorticity bands and so leads to a slower diffusion of the unstable regions and a slower decay in Ra^u. On the other hand, if Re increases through a decrease in ν while the shear layer velocity is fixed, it leads to an increase in Ra^u since $Ra^u \propto 1/\nu$. Figure 4(*c*) shows the effect of an increase in
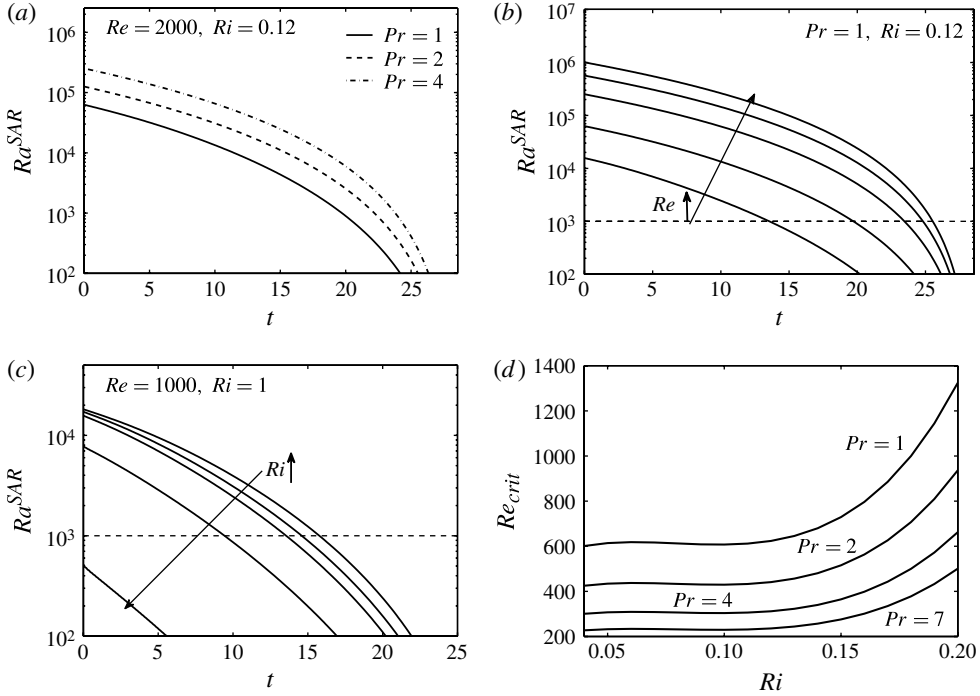
FIGURE 4. (*a*) Effect of *Pr* on the Ra^u for $Ri_0 = 0.12$ and $Re = 2000$; (*b*) effect of *Re* on Ra^u for $Pr = 1$ and $Ri_0 = 0.12$; here *Re* is increased in the direction of the arrow from 1000 to 2000, 4000, 6000 and 8000; (*c*) effect of Ri_0 on Ra^u for $Pr = 1$ and $Re = 1000$; here Ri_0 is increased in the direction of the arrow from 0.04 to 0.08, 0.12, 0.16 and 0.2; (*d*) critical *Re* at which Ra^u becomes equal to 1000 at t_m for various Prandtl number values. The horizontal axis in (*a–c*) represent time elapsed post t_m.

the Richardson number on Ra^u. Although at first glance (3.1) might suggest that an increase in Ri_0 should lead to an increase in Ra^u, the figure shows that this is clearly not the case. An increase in Ri_0 decreases Ra^u dramatically for two reasons: first, an increase in Ri_0 considerably increases the evolution time of the KH billows and leads to a significant decrease in $\Delta\rho^u$ by time t_m. Second, the maximum amplitude of the KH billow decreases as the stratification increases and this translates into a thinner unstable layer. As $Ra^u \propto (\delta^u)^3$, this effect leads to a highly significant decrease in Ra^u as Ri_0 increases.

It has been established in previous work (as reviewed in Peltier & Caulfield 2003) that the Reynolds number must exceed a critical value for the SCI to be physically realizable. To investigate the manner in which this critical value for *Re* changes with Ri_0 and *Pr*, figure 4(*d*) shows plots of the critical Reynolds number, Re_c, versus Ri_0 for various Prandtl numbers. To construct this diagram, we have calculated the minimum *Re* for which Ra^u exceeds 1000 at t_m. This must be considered a qualitative estimate of the occurrence of SCI for two reasons: first, it is an assumption that $Ra_c = 1000$ can be used as a critical value for overturning of the cores' unstable regions; second, Ra^u must in addition remain super-critical long enough to allow the SCI to evolve. The plot shows that the critical *Re* is not sensitive to Ri_0 for $Ri_0 < 0.1$. However, for higher stratification levels, the flow must be at a higher Reynolds number for the SCI to be effective. This is a consequence of the stabilizing effect of the

stratification on the SCI. Moreover, the figure shows that as the Prandtl number increases, the critical Re is reduced. Hence, one should be able to observe (in three-dimensional DNS simulations) a transition of the shear layer to turbulence through the convective instability at relatively low Reynolds number but at higher Prandtl numbers than those employed previously in three-dimensional simulations discussed in the literature. The $Pr = 1$ curve in figure 4(d) indicates that the critical Re is ~600 for $Ri_0 < 0.12$ which is in accord with the finding of earlier studies.

We focus next on the minimum Richardson number on the braid. Figure 5 provides plots of the calculated values of the braid Richardson number at the stagnation point over a two-dimensional Re–Ri_0 space for $Pr = 1, 2, 4$ and 7. The values of Ri_B are indicated on each line in the figures with the thick black line corresponding to $Ri_B = 0.25$. In agreement with (3.10), both an increase in Ri_0 (at constant Re) and an increase in Re (at constant Ri_0) lead to a decrease in Ri_B and increase the possibility of occurrence of the braid SSI. Comparison of all four frames shows that an increase in Pr (at fixed Re and Ri_0) leads to an increase in Ri_B, thus reducing the possibility of occurrence of the braid SSI. In other words, at a fixed Ri_0, the Reynolds number of the flow must be higher for a larger Prandtl number for the braid shear instability to be possible.

It was pointed out by Dritschel *et al.* (1991) and reinforced by Staquet (1995) that Ri_B is not an entirely adequate measure of the propensity of occurrence of SSI of the braid and that γ_s/Ω_s also needs to be smaller than some critical value. Therefore, we have plotted contours of γ_s/Ω_s in figure 5(f) of the figure and have also included results from our two-dimensional simulations as data points represented by stars for $Pr = 1$ in (a). Each star corresponds to a numerical simulation for which secondary vortices were actually observed in the two-dimensional simulation. The two encircled stars correspond to observation of secondary vortices on the braid which were not of SSI type and which will be further discussed in *MP2*. Please note that some of the simulations from which the starred data points in figure 5(a) are taken are not listed in table 1 since they have been used only for the purpose of constructing figure 5(a). There is a clear gap in the Ri_0–Re plane between the curve on which $Ri_B = 0.25$ and the actual formation of vortices on the braid (in figure 5a). It has already been discussed in Dritschel *et al.* (1991) that a rotation of a vorticity layer can suppress the growth of instabilities growing on the layer. Once the braid has attained an almost constant tilt angle, the shear instability has a limited time to emerge, otherwise other instabilities may take control of the transition process and modify the braid structure (e.g. the pairing instability) or destroy the organized flow structure required to support it (such as the three-dimensional SCI). Therefore, for some of the points in the gap between the thick line and the stars in figure 5(a), shear instability may have insufficient time to evolve.

Furthermore, as the cores expand with time, the strain field induced by the vorticity entrapped in them greatly suppresses emergence of the braid SSI while SCI can still be expected to emerge. Dritschel *et al.* (1991) studied an instability growing on an infinitely long tilted unstratified vorticity layer subjected to a pure strain field and proposed that a value of $\gamma_s/\Omega_s < 0.065$ is needed for shear instability to amplify at the stagnation point. This criterion was further investigated in the context of stratified shear layers in Staquet (1995). We will however argue in § 4.1 that the instability discussed in Dritschel *et al.* (1991) is not a shear instability and thus, $\gamma_s/\Omega_s < 0.065$ might not be a relevant criterion for braid shear instability in unstratified flow. Nevertheless, the strain field still acts so as to decrease the growth rate of the braid shear instability and γ_s/Ω can be treated as a rough measure for that. However, it is better to average γ_s/Ω_s over the extent of the braid. Comparing figure 5(a)
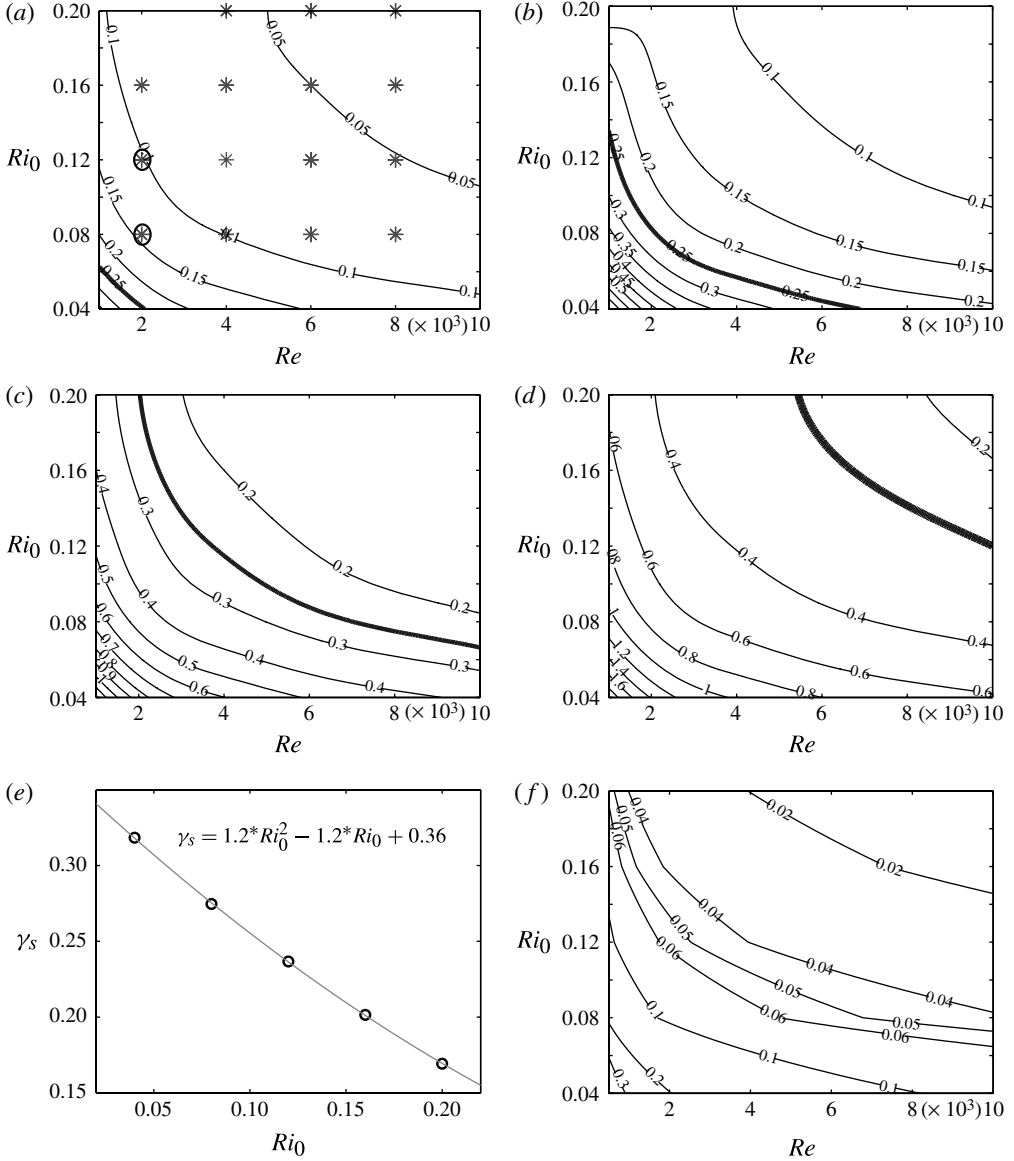
FIGURE 5. Plots of Ri_B at the braid stagnation point as a function of Reynolds number for: (*a*) $Pr = 1$; (*b*) $Pr = 2$; (*c*) $Pr = 4$; and (*d*) $Pr = 7$. Stars in (*a*) correspond to actual numerical simulations for which secondary vortices were observed on the braid. The heavy solid line in each frame marks the focus of points on which Ri_B equals the nominal critical value of braid instability of 0.25. (Note that the vertical axes are Ri_0 whereas the contours are for Ri_B.) (*e*) Strain rate at the stagnation point as a function of Ri_0. (*f*) Map of the γ_s/Ω_s contour in the Ri_0–Re parameter space for $Pr = 1$. The Ri_B contours in (*a*–*d*) are constructed by using (3.10), (3.9), (3.8) and $\Delta\rho_b = 2$. Panel (*e*) is made by using (3.8) and model of *CS76*. The second-order relation shown in the panel is a fit to the calculated data points. In (*f*) Ω is calculated from (3.6).

and (f) shows that SSI grows (non-encircled stars in figure 5a) for $\gamma_s/\Omega_s < 0.05$. The two panels together suggest that as Ri_0 is increased at a fixed Re, two factors lead to promotion of the SSI: first, the strain field weakens (due to reduced core size) and thus suppression of braid shear instability by the strain field diminishes; second, Ri_B reduces because of the increased shear in the braid due to enhanced baroclinic production of vorticity in the braid. For points in the stable regions (i.e. bottom left corners) of figure 5(a,f), either the braid is not shear unstable (due to large Ri_B) or perturbations cannot grow due to suppression by the strain field. For the latter case, if Re is sufficiently increased, perturbations will gain large enough growth rates to overcome the suppressing influence of the strain field.

These issues motivate our stability analyses in the following section. We will investigate the influence of stratification on various three-dimensional secondary instabilities in *MP2*. At this point we only point out that an increase in the stratification level decreases the strain field as shown in figure 5(e) (obtained using (3.8)) which shows a quadratic relation between the strain rate and Ri_0. Decreases in γ and Ri_B due to increase in Ri_0 both act in favour of emergence of braid shear instability and therefore SSI can emerge at much lower Reynolds numbers in agreement with figure 5(a). However, we show in the following section that the length of the braid which is susceptible to shear instability decreases rapidly during evolution of the KH wave due to growth of the vortex cores. This re-enforces the argument that any discussion of criteria for braid shear instability needs to take the full braid into account rather than just the structure of the braid at the stagnation point.

Based on figure 5, we may conclude that at a fixed Prandtl number, increases in Ri_0 and Re both promote the possibility of occurrence of the SSI on the braid by reducing both Ri_B and γ_s/Ω_s. And based on figure 4, we conclude that increase in Re enhances chances of secondary convective instability in the cores while increase in Ri_0 reduces its chances. Hence, at lower Reynolds numbers and in circumstances in which Ri_0 is small we can expect the dominance of the convective instability, while at larger Reynolds number with strong stratification, we can expect to see SSI. According to figure 4(a–d), as Pr increases, the region in Re–Ri_0 space of possible occurrence of the SSI is shifted to higher Reynolds numbers. As increase of Pr also promotes the probability of core convective instability, we conclude that increase in Pr (while keeping other parameters constant) increases the probability of SCI, and decreases the probability of SSI. Therefore, in salt-stratified shear layers where Pr is considerably larger than heat-stratified flows, one needs to be at much larger Reynolds numbers (compared with heat-stratified layers) for SSI to grow in abundance on the braid. This is in agreement with the observations of Geyer *et al.* (2010).

Horizontally infinite stratified shear layers with $Ri_B > 0.25$ are known to be susceptible to Holmboe instability provided that R_B, the ratio of the braid's vorticity layer thickness to that of its density layer thickness, is large enough (at least $\geqslant 2$). In *S03* it is shown that $R_B \simeq Pr^\alpha$ where $\alpha = 0.36$ for $1 < Pr < 7$. This suggests that we might expect Holmboe waves for $Pr \geqslant 7$ and $Ri_B > 0.25$ (the region to the right of the thick line in figure 5d) to arise on the braid. To provide an adequate investigation of this suggestion will however require further analysis which we will not pursue in the present paper.

4. Non-separable stability analysis of the KH wave

In this section, we discuss the methodology to be employed to test the stability of the two-dimensional nonlinear flow fields (obtained from numerical simulations)

to three-dimensional perturbations. The method we employ is that developed by *KP85* and employed previously by Smyth & Peltier (1991) and *CP00* as reviewed in Peltier & Caulfield (2003). This methodology is an extension of the earlier work of Clever & Busse (1974) on the stability of two-dimensional steady-state convection against three-dimensional perturbations. For additional details concerning the methodology, the reader is referred to *KP85*.

Beginning from the Boussinesq governing equations introduced in §2, we divide the total flow fields into a basic time-evolving two-dimensional state, which is represented by two-dimensional flow fields obtained from the DNS simulations, and three-dimensional perturbation fields. This decomposition may be written explicitly as

$$f(x, y, z, t) = \tilde{f}(x, z, t) + f'(x, y, z, t), \tag{4.1}$$

where f represents any one of the three components of the velocity field or the density or pressure field. The corresponding fields of the two-dimensional background KH wave are represented by $\tilde{f}$ and the three-dimensional perturbations to the background fields are represented by f'. Upon substitution of (4.1) into the governing equations, and linearizing in the three-dimensional fluctuations, the coefficients of the various perturbation terms in the resulting equations comprise the KH wave fields $\tilde{U}$, $\tilde{W}$ and $\tilde{\rho}$ and their derivatives. These coefficients are all independent of the cross-stream y-coordinate and are periodic in x with the same wavelength as the primary KH wave. Hence, based on the basic ideas of Floquet theory (e.g. Jordan & Smith 1977), we may separate the structures of the perturbation fields as

$$f'(x, y, z, t) = \epsilon \hat{f}(x, z, t) e^{i(bx+dy)}, \tag{4.2}$$

in which $\hat{f}(x, z, t)$ is periodic in x, ϵ is an ordering parameter and b and d are the streamwise and spanwise wavenumbers of the three-dimensional perturbations. Note that the total fields are periodic in x only if b is commensurate with λ, the wavenumber of the KH wave. Equation (4.2) may be further simplified by noting that experimental observations and high-resolution numerical simulations have shown that the secondary instabilities of interest to us grow to finite amplitude very quickly compared with the evolution of the original two-dimensional KH wave. Hence, we may assume that the flow evolves on two separate time scales, the slower being that of the background KH wave. We may therefore ignore the time dependance of the Floquet coefficients and (4.2) is reduced to the form:

$$f'(x, y, z, t) = \epsilon \hat{f}(x, z) e^{i(bx+dy)+\sigma t}, \tag{4.3}$$

where σ is the complex growth rate of the disturbances. This time separation is of course subject to justification *a posteriori*. Following *KP85*, the total fields $\tilde{f} + \hat{f} e^{i(bx+dy)+\sigma t}$ are substituted into the governing equations and the background two-dimensional field is subtracted to obtain linearized equations at order ϵ:

$$\sigma \hat{u} = -\tilde{U}(\partial_x + ib)\hat{u} - \tilde{W}\hat{u}_z - (\partial_x + ib)\tilde{U}\hat{u} - \tilde{U}_z\hat{w} - (\partial_x + ib)\hat{p} + Re^{-1}\nabla^2\hat{u}, \tag{4.4}$$

$$\sigma \hat{v} = -\tilde{U}(\partial_x + ib)\hat{v} - \tilde{W}\hat{v}_z - id\hat{p} + Re^{-1}\nabla^2\hat{v}, \tag{4.5}$$

$$\sigma \hat{w} = -\tilde{U}(\partial_x + ib)\hat{w} - \tilde{W}\hat{w}_z - (\partial_x + ib)\tilde{W}\hat{u} - \tilde{W}_z\hat{w} - \hat{p}_z + Ri\hat{\rho} + Re^{-1}\nabla^2\hat{w}, \tag{4.6}$$

$$\sigma \hat{\rho} = -\tilde{U}(\partial_x + ib)\hat{\rho} - \tilde{W}\hat{\rho}_z - (\partial_x + ib)\tilde{\rho}\hat{u} - \tilde{\rho}_z\hat{w} + (RePr)^{-1}\nabla^2\hat{\rho}, \tag{4.7}$$

$$0 = (\partial_x + ib)\hat{u} + id\hat{v} + \hat{w}_z, \tag{4.8}$$

where $\hat{u}$, $\hat{v}$, $\hat{w}$, $\hat{\rho}$ and $\hat{p}$ are the (x, z)-dependent parts of the streamwise, spanwise and vertical velocity, density and pressure perturbations, respectively. A diagnostic equation can be obtained for $\hat{p}$ by combining (4.4), (4.6) and (4.8) to obtain

$$\nabla^2 \hat{p} = Ri(\partial_x + ib)\hat{\rho} - 2((\partial_x + ib)\tilde{U}(\partial_x + ib)\hat{u} + \tilde{W}_z \hat{w}_z$$
$$+ (\partial_x + ib)\tilde{W}\hat{u}_z + \tilde{U}_z(\partial_x + ib)\hat{w}). \tag{4.9}$$

Replacing (4.8) with (4.9) decouples (4.5) from the rest of the system and we can solve (4.4), (4.6), (4.7) and (4.9) for $\hat{u}$, $\hat{w}$, $\hat{\rho}$ and $\hat{p}$. Either of the (4.5) or (4.8) may then be used to calculate $\hat{v}$ and the agreement between the two solutions for $\hat{v}$ can be employed as a measure of the accuracy of the calculations.

In order to convert the resulting equations into an eigensystem, the $(x - z)$ dependence of the solution fields are discretized using the Galerkin method. Details of the discretization as well as of the solution for the eigenvalues and selected eigenvectors are provided in the supplementary material (for original derivations refer to *KP85*). The truncation level, N, used for the Galerkin expansions is chosen using the truncation scheme of *KP85* (see equation $SM - (5.6)$ in the supplementary material for details). We choose $N = 37$ based on the limitations imposed by the resolutions of the numerical simulations used to provide the background flow information (see the supplementary material for details).

Once the eigenvalues (σ, b, d) are found, the dynamical processes that govern the evolution of a given disturbance may be diagnosed by means of the equation of the perturbation kinetic energy defined by

$$\mathscr{K}' = \langle (\hat{u}^* \hat{u} + \hat{v}^* \hat{v} + \hat{w}^* \hat{w}) \rangle, \tag{4.10}$$

where stars represent complex conjugate and angle brackets represent the integral

$$\langle \rangle = \frac{2\pi}{\lambda} \int_0^{2\pi/\lambda} \frac{2\pi}{d} \int_0^{2\pi/d} \int_0^{H_D} \mathrm{d}x \, \mathrm{d}y \, \mathrm{d}z, \tag{4.11}$$

where H_D is the domain height. The growth rate of the perturbation kinetic energy of a disturbance can be calculated following *KP85* by using

$$\sigma_r \simeq \frac{1}{2\mathscr{K}'} \frac{\mathrm{d}\mathscr{K}'}{\mathrm{d}t} = \mathscr{S}h + \mathscr{S}t + Ri\mathscr{H} + \mathscr{D}/Re, \tag{4.12}$$

where the terms on the right-hand side represent the contributions to the growth rate of the perturbation kinetic energy $\mathscr{K}'$ due to the shearing $(\mathscr{S}h)$ and straining $(\mathscr{S}t)$ deformations of the basic two-dimensional velocity field, convection associated with unstable density gradients $(\mathscr{H})$, and viscous dissipation $(\mathscr{D})$. Explicit expressions for these terms are

$$\mathscr{S}h = -\langle (\tilde{W}_x + \tilde{U}_z)(\hat{u}^* \hat{w})_r \rangle / \mathscr{K}', \tag{4.13a}$$

$$\mathscr{S}t = -\langle \tfrac{1}{2}(\tilde{U}_x - \tilde{W}_z)(\hat{u}^* \hat{u} - \hat{w}^* \hat{w}) \rangle / \mathscr{K}', \tag{4.13b}$$

$$\mathscr{H} = \langle (\hat{w}^* \hat{\rho})_r \rangle / \mathscr{K}', \tag{4.13c}$$

$$\mathscr{D} = \langle (\hat{u}^* \nabla^2 \hat{u} + \hat{v}^* \nabla^2 \hat{v} + \hat{w}^* \nabla^2 \hat{w})_r \rangle / \mathscr{K}', \tag{4.13d}$$

where $\tilde{U}$ and $\tilde{W}$ are the streamwise and vertical velocity components of the background two-dimensional flow (represented by $\tilde{f}$ in (4.1)) and the quantities denoted by '$\hat{}$' are the perturbation fields.

Prior to presenting the results obtained by the application of this methodology in the following subsection, we require an estimate of the growth rate of the original

KH wave, σ_{KH}. This is required to enable a rigorous *a posteriori* justification for the assumed separation of time scales between that which governs the evolution of the background state and that which governs the evolution of the perturbations superimposed upon it. The requirement of a time scale separation may be represented as

$$|\sigma_{KH}| \ll \sigma_r. \tag{4.14}$$

Although we will not pursue this slightly more sophisticated method of analysis herein, in circumstances in which the separation of time scales is questionable one may invoke the time-averaged stability matrix methodology of Smyth & Peltier (1994) to perform an optimal instability analysis that takes into account the influence of the temporal variations in the basic state KH wave upon the secondary instability process. Analogous to (4.12), σ_{KH} can be calculated using

$$\sigma_{KH} = \frac{1}{2\mathscr{K}_{KH}} \frac{\mathrm{d}}{\mathrm{d}t} \mathscr{K}_{KH} \tag{4.15}$$

where $\mathscr{K}_{KH}$ is the evolving kinetic energy of the background KH wave which may be represented non-dimensionally as

$$\mathscr{K}_{KH} = \langle (\tilde{U}^2 + \tilde{W}^2)/2 \rangle_{xz}, \tag{4.16}$$

in which $\langle \rangle_{xz}$ denotes integration over the x and z directions only. The background KH velocities $\tilde{U}$ and $\tilde{W}$ at each point of the domain can be obtained from our two-dimensional simulations using

$$\tilde{U} = u - \bar{u} \quad \text{and} \quad \tilde{W} = w - \bar{w}, \tag{4.17}$$

where ( ) denotes averaging in the streamwise direction and u and v are the total velocities. The total kinetic energy in the two-dimensional simulation domain is simply

$$\mathscr{K} = \langle [(u^2 + w^2)/2] \rangle_{xz}, \tag{4.18}$$

which itself may be subdivided into two components as

$$\mathscr{K} = \bar{\mathscr{K}} + \mathscr{K}_{KH}, \tag{4.19}$$

in which the first term on the right-hand side is the average kinetic energy of the evolving mean, background flow defined as

$$\bar{\mathscr{K}} = \langle \bar{u}^2/2 \rangle_z, \tag{4.20}$$

and the second term on the right-hand side of (4.19) is the kinetic energy associated with the spanwise-averaged two-dimensional perturbation (defined in (4.16)).

4.1. *Stability analysis for the case c1-1000-0.12*

In this section, we describe the results of the stability analysis for a marginal case located in the gap between the $Ri_B = 0.25$ line and the starred points in figure 5(*a*). Specifically, we choose the case with $Pr = 1$, $Re = 1000$ and $Ri_0 = 0.12$. This marginal case is chosen since it has a braid Richardson number small enough to expect secondary vortices to form on the braid and yet such vortices do not form in the actual two-dimensional simulation due to influence of the strain field. Our main goal is to quantify the influence of the vortex cores on the spatial extent and growth rate of the braid shear instability.

Figure 6 shows the vorticity field for various times in the flow evolution and figure 7 shows the corresponding plots of the flow diagnostics. Time $t = 60$ is the time when
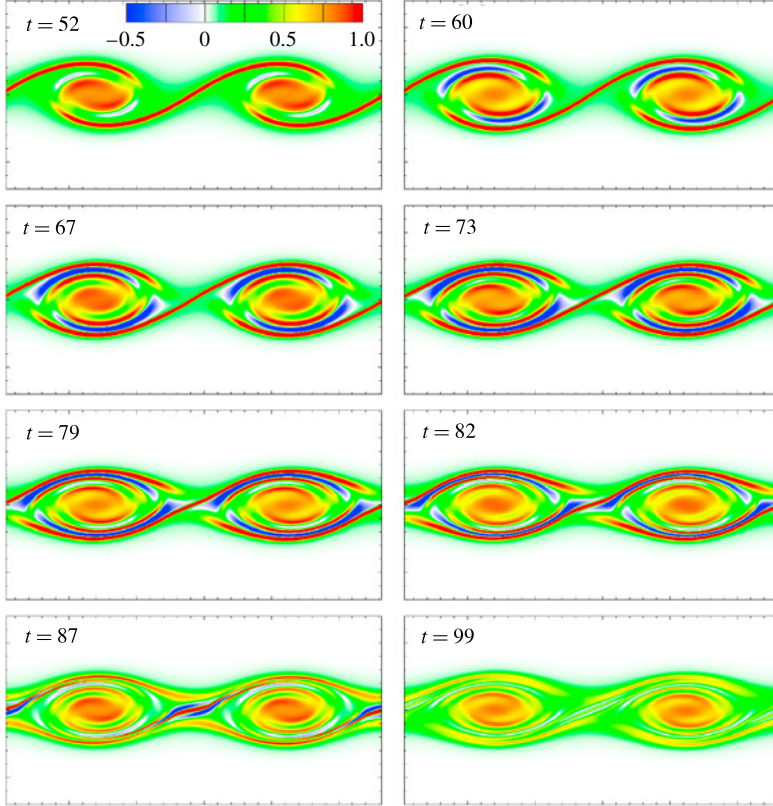
FIGURE 6. Vorticity contours at various stages of flow evolution for case $c1$-1000-0.12. The horizontal and vertical axes represent x (for $0 < x < 28.5$) and z (for $3 < z < 17$), respectively.

the kinetic energy of the KH wave, $\mathcal{K}_{KH}$, reaches a peak (seen in figure 7b). This time will be referred to as the time of 'climax' (denoted by t^*) of the primary two-dimensional KH instability. Up to this point, the shear layer has rolled-up into a spatially periodic sequence of growing cores leading to an increase in the total potential energy of the system at the cost of the total kinetic energy.

The blue vorticity bands shown in figure 6 coincide with the unstable regions inside the cores. At time $t = 52$, the first pair of unstable regions begin to form. Figure 7(c) depicts the evolution of the corresponding Ra^u which grows with time, reaches a maximum, and then decreases as both the δ^u and $\Delta\rho^u$ decrease with time. We expect the possibility of the shear-aligned convective instability (in a similar case, but in a three-dimensional flow) to follow essentially the same evolutionary history as does Ra^u.

Figure 7(d) shows evolution of the streamwise distance between the tips of the outer most unstable regions in the two neighbouring cores, δ_{pair}. This demonstrates that the two main vorticity bands in the neighbouring cores meet at a time close to $t = 80$. At approximately the same time, the flow is deformed in the vicinity of the stagnation point. This is a consequence of the change of the velocity field near the stagnation point due to the advance of the thick vorticity bands in the cores. We will return to further discuss this point shortly. It appears that the close encounter of vorticity bands
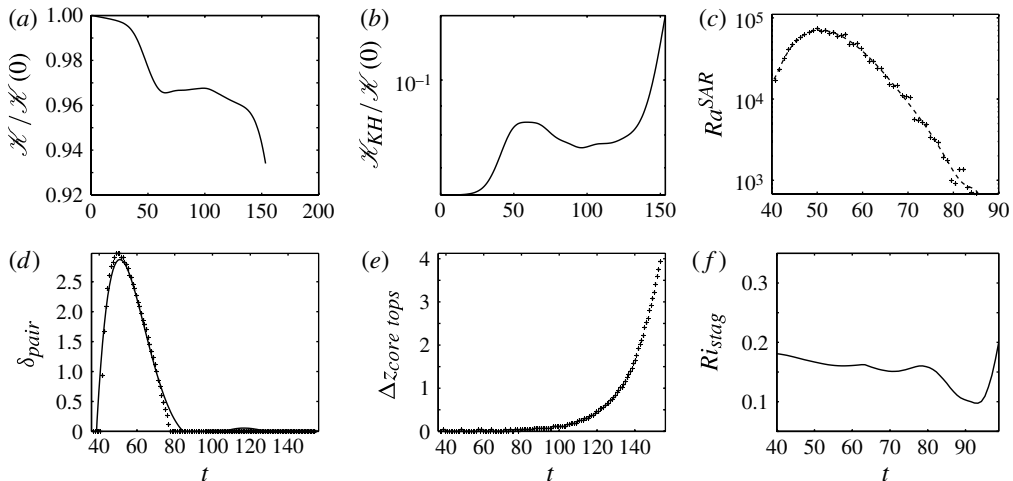
FIGURE 7. Time evolution of: (*a*) total kinetic energy $\mathcal{K}$ normalized by its value at $t = 0$; (*b*) kinetic energy of the nonlinear KH wave $\mathcal{K}_{KH}$ normalized by $\mathcal{K}(0)$; (*c*) Ra^u; (*d*) δ_{pair}; (*e*) Δz_{cores}; and (*e*) the stagnation point Richardson number on the braid, Ri_B^{stag}.

in the cores with the stagnation point perturbs the flow structure and affects the strain field at the stagnation point. As this strain field is essential for maintaining the general structure of the KH wave, its modification marks the beginning of the pairing process. This is shown by figure 7(*e*) in which we have plotted the absolute value of the difference between the maximum height of the upper surface of the two neighbouring vorticity cores in the wave train, Δz_{cores}. The growth of this parameter to values larger than zero indicates the onset of the pairing process.

Once the pairing process begins, it is followed initially by complete draining of braid vorticity (at $t = 99$ in figure 6) and subsequently by formation of a new braid. The pairing process leads to a second period of dramatic increase in the kinetic energy of the two-dimensional wave ($\mathcal{K}_{KH}$) as shown in figure 7(*b*). This is accompanied by a further rise in the potential energy of the system due to the coalescence of the two cores and hence the total kinetic energy of the system undergoes a secondary fall (figure 7*a*). Figure 7(*f*) shows the evolution of Ri_B at the stagnation point. Even though it has a value below 0.25, no SSI is observed prior to pairing. Although secondary vortices do form on the braid after the two-dimensional pairing process is completed (not shown in the figures), we are not concerned with them at this stage of flow evolution as we suspect that in a three-dimensional flow, three-dimensional instabilities will most probably have already occurred, thus rendering the paired basic state physically meaningless. Figure 7(*f*) demonstrates that Ri_B decreases to 0.1 during the phase of braid deformation ($t = 80$–100) which might suggest a greater chance for the shear instability to onset. However, that possibility is suppressed in this case by the onset of the pairing process. As we show in the companion paper *MP2*, at higher Reynolds numbers the braid deformation may amplify much earlier thereby allowing secondary vortices to develop prior to pairing.

We begin our secondary stability analysis for this case at the climax time ($t^* = 60$). At this time, the cores have not grown overly large so as to impinge upon the stagnation point and there is an extended length of braid which might be susceptible to SSI. Figure 8 shows the perturbation kinetic energy and density eigenfunctions for
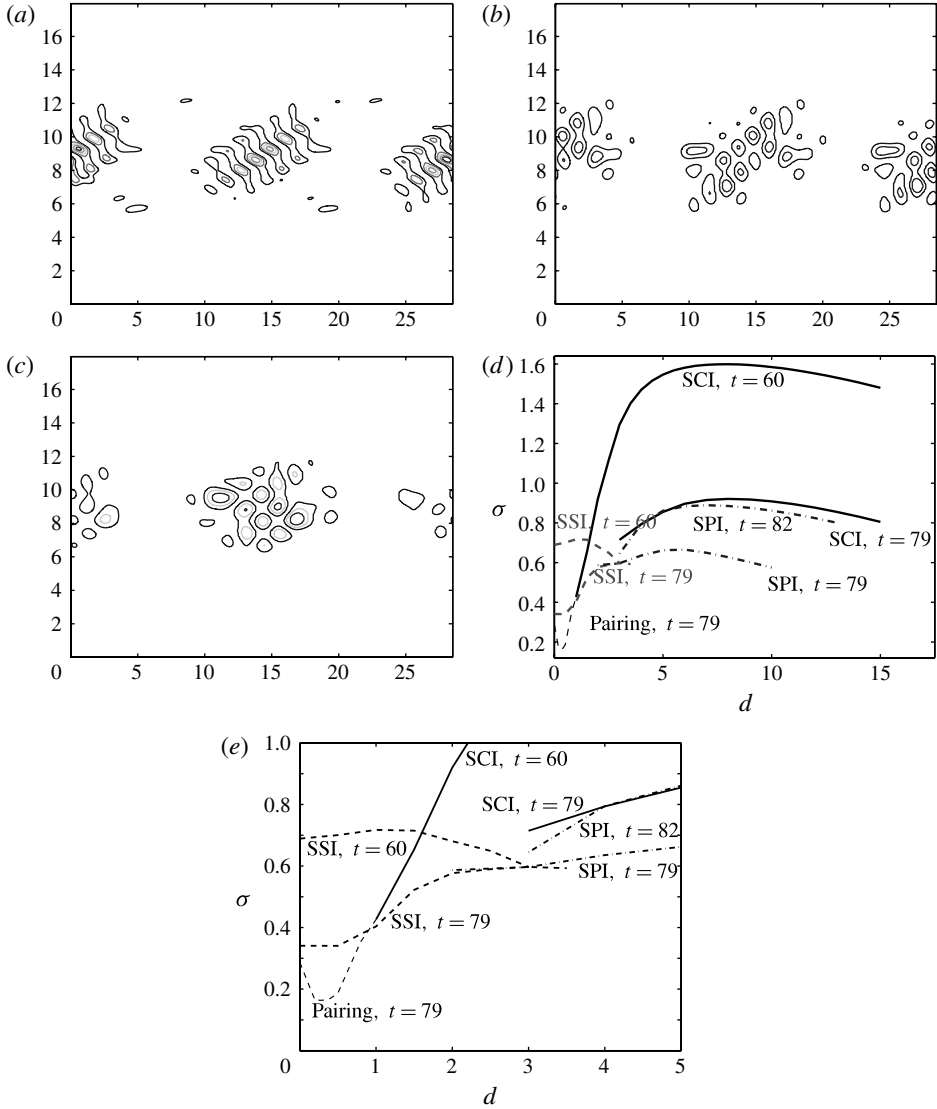
FIGURE 8. (*a*) The perturbation kinetic energy eigenfunction, $\mathcal{K}'$; (*b*) density eigenfunction for the SSI with $d = 0$ and for the time $t^* = 60$; (*c*) the density eigenfunction for the $d = 0$ SSI mode at $t = 67$; (*d*) growth rate versus the spanwise wavenumber d for the SSI mode at $t = 60$ and $t = 79$ (dashed lines), the SCI mode at $t = 60$ and $t = 79$ (solid lines), the SPI mode at $t = 79$ and $t = 82$ (dashed-dotted line) and the pairing mode (thin dashed line in the bottom left corner of the plot); (*e*) same as (*d*) but zoomed over the $(0 < \sigma < 1, 0 < d < 0.5)$ range. The horizontal and vertical axes in the panels correspond to x and z, respectively, and can be used to make comparisons with figure 6.

the fastest growing mode at time 60 for $d = 0$ (i.e. two-dimensional perturbations). The $\mathcal{K}'$ eigenfunction shows that the mode is centred precisely on the braid and has a braid streamwise wavelength of 1.38 (wavenumber of 4.56) near the stagnation point. It also has a growth rate of $\sigma_r = 0.69$. The wavelength is ~ 4.6 times the braid thickness at the stagnation point which is smaller (due to the action of the

strain field) than the factor of ~ 7 corresponding to infinite horizontal shear layers. The wavenumber and the growth rate are close to those found by *S03* by performing secondary stability analysis for an infinitely long tilted vorticity filament. We expect the flow field induced by the growing cores to considerably affect the eigenfunctions of this mode during flow evolution. The next few fastest growing modes of instability for $d = 0$ are all found to be similar to that shown in figure 8 but with slightly smaller growth rates and different braid streamwise wavenumbers. To the best of the authors' knowledge, SSI has always been assumed to be two dimensional (as might be suggested by a simple extension of Squire's (1933) theorem). However, according to our analysis, unstable modes also exist for $d > 0$ and hence SSI is of a three-dimensional nature. Figure 8(d) shows the variation in the growth rate of the fastest growing mode of SSI with variations in the wavenumber, d, for $t = 60, 79$. Although at $t = 60$ the SSI seems to have the fastest growth rate at $d \sim 0$, at $t = 79$ its growth rate increases with d and there seems to be a high-wavenumber cut-off limit at $d \sim 4$. It should be noted that Squire's theorem applies to parallel flows and therefore should not be extended to the braid of a KH billow which is subject to a strain field. Even for a parallel shear flow, there are circumstances in which Squire's theorem permits the possibility of the flow bifurcating directly to a three-dimensional state (see Smyth & Peltier (1990) for an example). Since the fastest growing mode is of long wavelength (having a wavelength comparable to the background KH wave), a long spanwise domain extent is required for three-dimensional simulations to capture it. As SSI has maximum growth rate at d close to zero, similar to pairing instability it is most likely to arise as a two-dimensional structure unless there are long-wavelength spanwise perturbations in the system. It has been shown in the literature (Ashurst & Meiburg 1988 and Cortesi *et al.* 1998, among others) that even very small amplitude spanwise perturbations of proper wavelengths can lead to three-dimensional pairing. It will be interesting to further investigate, through three-dimensional simulations, the role of spanwise perturbations on SSI.

Even though our stability analyses reveal the SSI modes, they are not realized in our two-dimensional simulation shown in figure 6. To demonstrate the reason for this, we track evolution of the SSI for various times during flow evolution ($50 < t < 90$) by repeating the stability analysis. The result is illustrated in figure 17 by the solid line with open circles which establishes that as the cores grow in the streamwise direction beyond the climax time, the growth rate of the SSI mode diminishes. Moreover, the along-braid extent of the SSI modes decreases with time beyond t^*. This can be seen by comparing figure 8(e), which shows the density eigenfunction for the $d = 0$ SSI mode at $t = 67$, with figure 8(b) for $t = 60$. The same is true for the $d > 0$ SSI modes as can be seen in figure 8 by noting that the family of SSI modes have larger growth rates at $t = 60$ compared with $t = 79$ (figure 8d). The continuous decrease in the growth rate and spatial extent of the instability with time strongly reduces the probability of formation of vortices on the braid. We suggest that this is the reason behind the 'gap' in figure 5(a).

Next we turn our attention to the braid deformation at the stagnation point. In figure 9, we overlay the vorticity contours with instantaneous streamlines for a sequence of times from $t = 67$ to $t = 82$. The Ri_B contours are also shown on the same figure for $t = 79$ and 87. As the outermost vorticity bands in the cores (blue bands) approach the stagnation point, the streamlines adjacent to the braid are deformed and stretched towards the vorticity bands due to the velocity field induced by the negative vorticity in the bands. By $t = 79$, the streamlines are significantly deformed compared with their initial orientation and a small recirculating region forms in the middle of
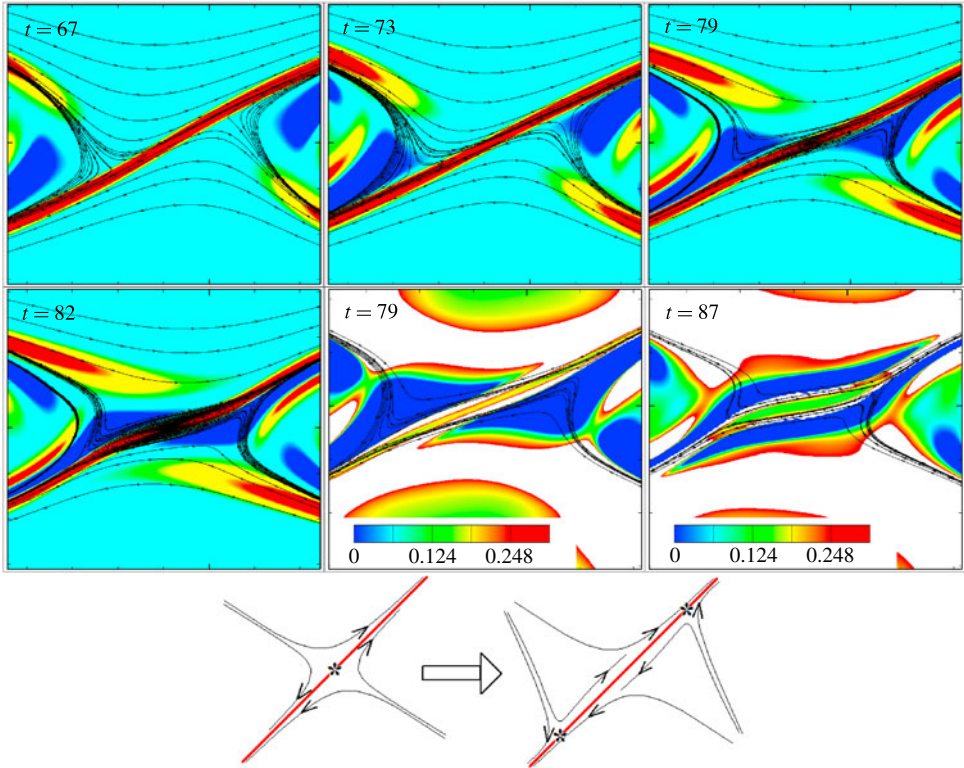
FIGURE 9. The top row and the left panel of the bottom row show the vorticity contours overlaid by the streamlines zoomed on the stagnation point. The contour levels are similar to figure 6. The centre and right figure in the middle row show the contours of the braid Richardson number overlaid by streamlines. Any region with $Ri_B > 0.25$ is whited out. The final row is a schematic plot which shows the streamlines before and after the core vorticity bands have made the stagnation point to split into two and move further away from the middle of the braid.

the braid. This region reaches a maximum strength at $t = 82$ before dissipation due to draining of the vorticity from the braid as the vorticity bands of the cores completely surround the braid. As mentioned earlier, this draining event also marks the onset of the pairing instability. To better understand how the streamline deformation leads to the emergence of the recirculating region, a schematic plot is also included in the bottom row of figure 9 which shows that at earlier stages in the evolution of the flow the streamlines have the form of a pure strain field. However, as the streamlines become deformed due to the influence of the approaching cores, the stagnation point is split as indicated by the stars in the schematic. The velocity field along the braid takes the form of a to-the-right and upward flow on the upper surface of the braid and a to-the-left and downward flow on the lower surface of the braid. This makes it possible for a recirculating region to form between the two starred points. Even though this region dies out fairly rapidly in this case, we show in *MP2* that in certain circumstances it may grow so significantly as to produce important modifications of the flow, including both the braid and the core.

To better understand the effect of the braid deformation on the global structure of the KH billows, we have performed additional stability analyses for $t = 80$ and $t = 87$.
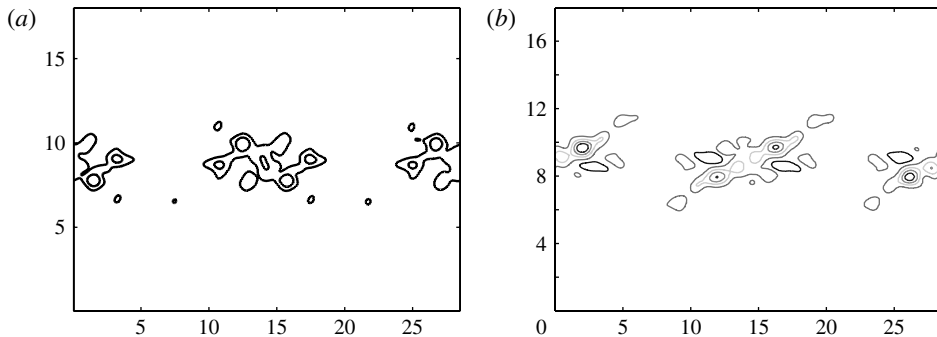
FIGURE 10. The density eigenfunction for: (*a*) the fastest growing mode $d = 0$ mode of the SVBI at $t = 80$; and (*b*) the fastest growing two-dimensional mode at $t = 87$. (Note that *b* does NOT represent the SVBI.)

The fastest growing mode for $t = 80$ is shown in figure 10(*a*). The instability is not limited to the braid and it also affects the vorticity bands in the core. This can lead to formation of isolated vortices inside the cores as shown by the fastest growing mode of instability at $t = 87$ in figure 10(*b*). The formation of these vortices, together with the formation of the recirculating region in the middle of the braid have been previously reported in the simulations of Staquet (1995). We refer to this instability as the secondary vorticity band instability (SVBI) since it is triggered by the fusing of the vorticity bands inside the core. This instability has a much shorter lifetime and smaller growth rate compared with the SCI.

The maps of Ri_B in figure 9 establish that during the period of braid deformation, the portion of the braid in which $Ri_B < 0.25$ is limited to the deforming section around the stagnation point. The two maps show that Ri_B decreases with time in the deforming region and tends to zero as the braid vorticity is drained. This rapid decrease in Ri_B renders the region more susceptible to shear instability. Figure 10(*b*) establishes the possibility of formation of two vortices at the tips of the deformed braid region shown in figure 9. Our simulation demonstrates that this does not occur as the pairing process dominates. However, if the pairing process were retarded, we would expect that the vortices would form. This happens in a similar case but for $Re = 2000$ as shown for case $c1$-2000-0.12 in the supplementary material and further discussed in *MP2*.

Figure 8(*d*) shows that for small values of d and at early stages of flow evolution, SSI modes are dominant insofar as their growth rates are concerned. However, for d sufficiently large, secondary three-dimensional convective instabilities are predicted by the stability analysis. The structure of the convective modes along with their finite-time evolution has been studied in detail in *KP85* and *CP00* and hence will not be discussed here. It suffices to say that unlike the SSI group, the SCI modes are oscillatory. In figure 8(*d*) we have plotted the variations of the growth rate versus the spanwise wavenumber d for the fastest growing SCI mode for times 60 and 79. For $d < 2$, the SSI modes dominate at $t = 60$ while for larger values of d the SCI mode dominates by a wide margin. This domination continues for an extended period of time as is established by comparing the $t = 79$ SSI and SCI curves in figure 8(*d*).

Another oscillatory secondary instability supported by the evolving basic state KH wave is the pairing instability, the two-dimensional version of which was discussed in detail in *KP89*. We have found a continuous range of small wavenumbers for which
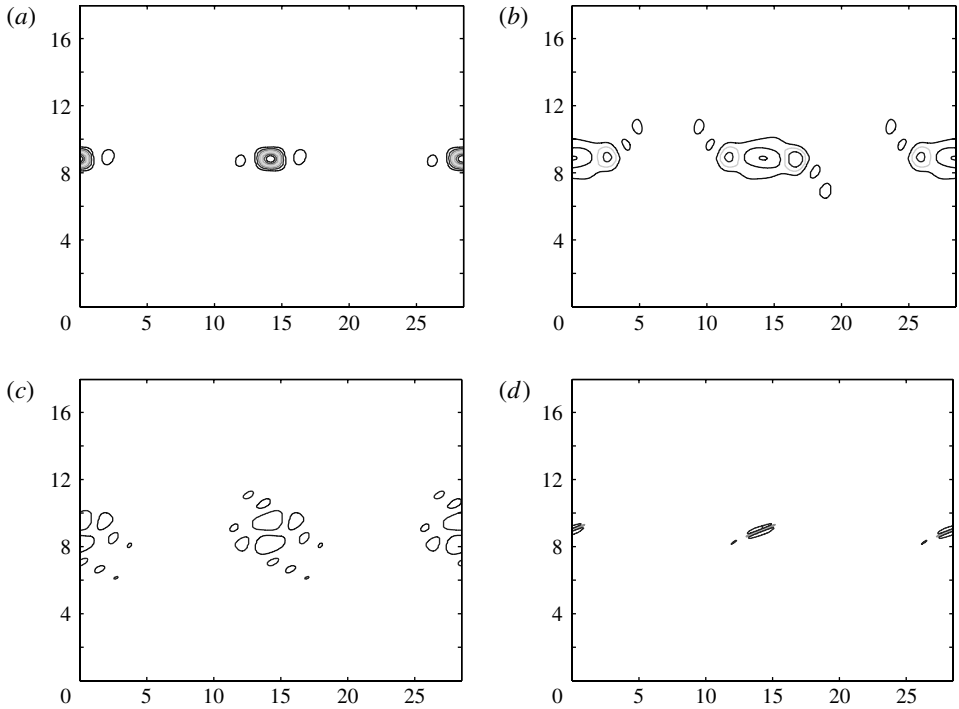
FIGURE 11. (*a*) The perturbation kinetic energy eigenfunction, $\mathscr{K}'$; (*b*) density eigenfunction; (*c*) vorticity eigenfunction; and (*d*) $\mathscr{S}h$ eigenfunction for the fastest growing mode of SPI with $d = 7$ and for the time $t = 82$.

pairing can occur. The thick solid line in figure 8(*d*) shows the corresponding growth rate curve for the pairing modes. The fastest growing mode is the two-dimensional pairing mode ($d = 0$) and a high-wavenumber cut-off limit of $d \sim 1$ is found by our analyses. The three-dimensional nature of the pairing instability has already been pointed out in the theoretical studies of Pierrehumbert & Widnall (1982) and Smyth & Peltier (1994) for homogeneous shear layers. Our analyses extend this result to stratified shear layers. As pointed out by Pierrehumbert & Widnall (1982), $d > 0$ pairing modes can lead to 'helical' or 'localized' pairing of vortex cores. The pairing mode retains a growth rate close to its early values for an extended period of time. In most of our two-dimensional simulations, it ultimately leads to an actual pairing of the cores. A fundamental issue is under what circumstances pairing may be entirely prevented, it being unusual in the high-Reynolds-number circumstances characteristic of the atmosphere and oceans.

The final instability revealed by our analyses for this case is one which is also three dimensional. Figure 11 illustrates several of the eigenfunctions for this instability at time $t = 82$. This mode is composed of a single localized counter-rotating pair of vortices that surround the stagnation point. The growth rate of this family of modes is independent of the streamwise wavenumber (parameter *b*) and so their structure may vary from one braid to the next. For example, the instability might occur only on every other braid etc. Since this mode is localized on the stagnation point, we refer to it as the secondary stagnation point instability (SPI). As will be discussed in detail shortly, this mode emerges due to the action of the strain field induced by the

vortex cores on the braid. Unlike SVBI, however, this mode is local to the stagnation point. There is a continuous range of spanwise wavenumbers over which the SPI exists. Figure 8(*d*) plots the variations of the growth rate versus *d* for times 79 and 82. Both curves show a peak around $d = 7$ which is close to the value of $d = 8.5$ corresponding to the fastest growing mode of the convective instability of the core. Comparing the two curves shows that the strength of the instability increases rapidly over a very short period of time. Near time $t = 80$, the fastest growing SPI mode has a larger growth rate than the fastest growing SCI mode. On this basis we suggest that if, in a three-dimensional flow, onset of the SCI has yet to occur, the SPI would have a significantly better chance of emerging compared to all of the other instabilities we have identified. The SPI modes shown in figure 11 emerge in our stability analysis once the cores have grown large and their outermost unstable regions have become extended close to the stagnation point. As the growth rate of the SPI shows little sensitivity to the spanwise wavenumber for large wavenumbers, similar to the SCI this mode is capable of injecting energy into small-scales facilitating a transition to turbulence.

This mode and its distinction from the SSI was briefly noted in *KP89* for $Re = 300$. However, further investigation of the mode was not pursued in that study due to the insufficient degree of convergence of its eigenfunction and also because of its considerably smaller growth rate compared with the SCI at the low Reynolds number of 300. Note that the two SPI $(\sigma - d)$ curves in figure 8(*d*) do not extend to $d = 0$ (while *KP89* reported this mode only for $d = 0$) because at small values of *d*, SSI modes dominate the hierarchy of eigenvalues, making the detection of SPI at $d = 0$ difficult. SSI modes did not exist at the low Reynolds number considered in *KP89*. There are two major differences between SPI and SSI. First, SPI is local to the stagnation point whereas SSI vortices are advected (upon formation) by the braid velocity field towards the vortex cores. Second, SPI is a highly three-dimensional mode with large growth rates at high wavenumbers whereas SSI is a long wave mode which will most probably develop in a two-dimensional fashion unless there is appropriate spanwise perturbations and the flow domain extends sufficiently large in the spanwise direction.

To further analyse the evolution of SSI and SPI, we need to study the contributions made to the growth rates of their perturbation kinetic energy $\mathcal{K}'$ due to the shearing $(\mathcal{S}h)$ and straining $(\mathcal{S}t)$ deformations of the basic two-dimensional velocity field, convection associated with unstable density gradients $(\mathcal{H})$ and viscous dissipation $(\mathcal{D})$, all introduced in (4.12) and (4.13). As both instabilities are local to the braid, it is important that we calculate the shear and straining contributions to their growth in a reference frame aligned with the braid. Therefore, we define a right-handed local co-ordinate systems attached to the braid at the stagnation point and with the *x*-axis aligned with the braid and the *z*-axis normal to the braid. For the purpose of transformation to this braid coordinate system, the global coordinate system is denoted by *X*–*Z*. Here *u* and *w* refer to velocities in the braid local coordinate system while *U* and *W* refer to those in the global coordinate system. The quantities in the two coordinates are related through

$$U = u\cos\psi - w\sin\psi, \quad W = u\sin\psi + w\cos\psi, \tag{4.21}$$

$$u = U\cos\psi + W\sin\psi, \quad w = -U\sin\psi + W\cos\psi, \tag{4.22}$$

$$X = x\cos\psi - z\sin\psi, \quad Z = x\sin\psi + z\cos\psi, \tag{4.23}$$

where, as before, ψ is the braid tilt angle.

Consistent with our formulation of the stability problem, '˜' and 'ˆ' will refer to background flow and perturbation field quantities in what follows. From (4.13) the normalized (by $\mathscr{K}'$) eigenfunction of the shearing and straining contributions of the background flow to an instability are

$$\text{Shear}_{eig} = -(\tilde{W}_X + \tilde{U}_Z)(\hat{U}^*\hat{W})_r/\mathscr{K}', \tag{4.24}$$

$$\text{Strain}_{eig} = -\tfrac{1}{2}(\tilde{U}_X - \tilde{W}_Z)(\hat{U}^*\hat{U} - \hat{W}^*\hat{W})/\mathscr{K}'. \tag{4.25}$$

Substituting (4.21) and (4.22) in (4.24) and (4.25) and using (4.23), it follows that the normalized shearing and straining contributions of the background flow to the eigenfunction of an instability in the braid reference frame become

$$\text{Shear}_{eig}^{braid} = -\frac{1}{\mathscr{K}'}\left(\mathscr{F}\cos\psi - \frac{\mathscr{G}}{2}\sin\psi\right)(\tilde{w}_x + \tilde{u}_z)$$

$$= \left(\frac{\sin\psi}{2\mathscr{F}} + \frac{\cos\psi}{\mathscr{G}}\right)(2\sin\psi\,\mathscr{F}\,\text{Strain}_{eig} - \cos\psi\,\mathscr{G}\,\text{Shear}_{eig}) \tag{4.26}$$

$$\text{Strain}_{eig}^{braid} = -\frac{1}{\mathscr{K}'}\left(\mathscr{F}\sin\psi + \frac{\mathscr{G}}{2}\cos\psi\right)(\tilde{u}_x - \tilde{w}_z)$$

$$= \left(\frac{\sin\psi}{\mathscr{G}} + \frac{\cos\psi}{2\mathscr{F}}\right)(\sin\psi\,\mathscr{G}\,\text{Shear}_{eig} + 2\cos\psi\,\mathscr{F}\,\text{Strain}_{eig}), \tag{4.27}$$

where

$$\mathscr{G} = (\hat{u}^*\hat{u} - \hat{w}^*\hat{w})\cos(2\psi) - (\hat{u}\hat{w}^* + \hat{u}^*\hat{w})\sin(2\psi), \tag{4.28}$$

$$\mathscr{F} = [\tfrac{1}{2}(\hat{u}^*\hat{u} - \hat{w}^*\hat{w})\sin(2\psi) + (\hat{u}^*\hat{w}\cos(\psi)^2 - \hat{u}\hat{w}^*\sin(\psi)^2)]_r. \tag{4.29}$$

As the buoyancy flux and dissipation terms in (4.12) are independent of the choice of coordinate system, sum of the shearing and straining terms will also be independent of choice of the coordinate system and so by combining (4.26) and (4.27) we get

$$\text{Shear}_{eig} + \text{Strain}_{eig} = \text{Shear}_{eig}^{braid} + \text{Strain}_{eig}^{braid}. \tag{4.30}$$

The shearing and straining contributions of the background flow to the growth rate of an instability can be calculated form:

$$\mathscr{S}h_b = \langle\text{Shear}_{eig}^{braid}\rangle_{xz}, \quad \mathscr{S}t_b = \langle\text{Strain}_{eig}^{braid}\rangle_{xz}, \tag{4.31}$$

and again we note that $\mathscr{S}h_b + \mathscr{S}t_b = \mathscr{S}h + \mathscr{S}t$.

Figure 12 shows contours of $\text{Shear}_{eig}^{braid}$ and $\text{Strain}_{eig}^{braid}$ for the climax time $t^* = 60$ and $t = 67$ for the SSI. The negative contribution from $\mathscr{D}$ was less than 2 % of σ_r at all times and the contribution from $\mathscr{H}$ was negligible. The figure shows that the SSI is almost entirely driven by the velocity shear in the braid while the strain field act so as to suppress the instability. Comparing figure 12(b) and (d) shows that the suppressing influence of the strain field grows both in magnitude and spatial extent along the braid while $\mathscr{S}h_b$ decreases with time. This increasing suppression leads to total elimination of the possibility of emergence of SSI by $t = 82$. This is shown in the table in figure 12 by providing the relative ratio of $\mathscr{S}h_b$ to $\mathscr{S}t_b$. The value of the ratio near -1 at $t = 82$ corresponds to a growth rate of nearly zero as $\sigma_r \sim \mathscr{S}h_b + \mathscr{S}t_b \sim 0$. The rapid increase in $|\mathscr{S}t_b/\mathscr{S}h_b|$ with time for the case under consideration explains the lack of formation of secondary vortices on the braid in the two-dimensional simulation which provided the background flow for the stability analyses. For the SSI to emerge in the form of a number of vortices on the braid, the Reynolds number
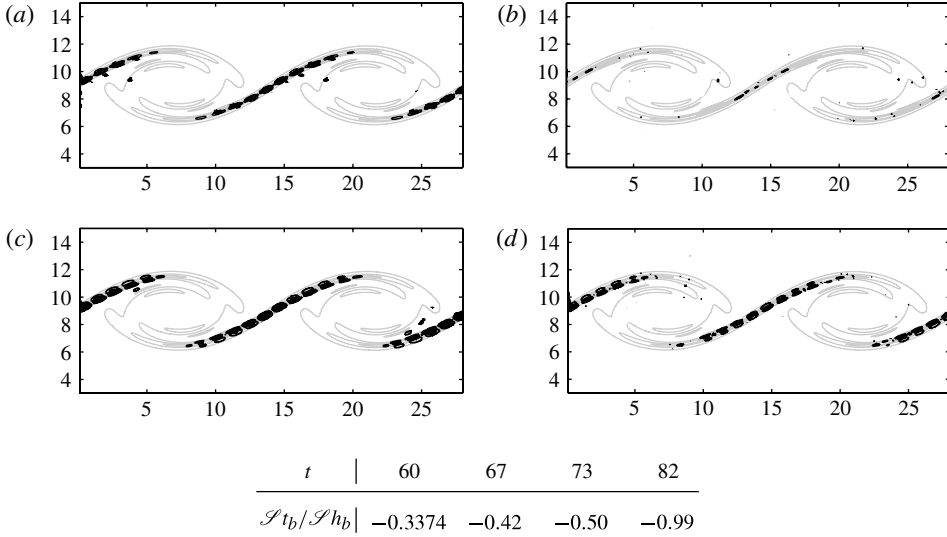
t	60	67	73	82
$\mathscr{S}t_b/\mathscr{S}h_b$	-0.3374	-0.42	-0.50	-0.99

FIGURE 12. Contours of $\text{Shear}_{eig}^{braid}$ and $\text{Strain}_{eig}^{braid}$ for the SSI of the braid at $t = 60$ and $t = 67$: (*a*) $\text{Shear}_{eig}^{braid}$ contour for SSI at $t = 60$, $\sigma_r = 1.0$, $\mathscr{S}h_b = 1.63$, $\mathscr{S}t_b = -0.55$; (*b*) $\text{Strain}_{eig}^{braid}$ contour for SSI at $t = 60$, $\sigma_r = 1.0$, $\mathscr{S}h_b = 1.63$, $\mathscr{S}t_b = -0.55$; (*c*) $\text{Shear}_{eig}^{braid}$ contour for SSI at $t = 67$, $\sigma_r = 0.51$, $\mathscr{S}h_b = 0.93$, $\mathscr{S}t_b = -0.40$; (*d*) $\text{Strain}_{eig}^{braid}$ contour for SSI at $t = 67$, $\sigma_r = 0.51$, $\mathscr{S}h_b = 0.93$, $\mathscr{S}t_b = -0.40$. The table shows the increase with time of the negative relative influence of strain field on the growth of the SSI.

needs to be sufficiently high (the critical point depending on both Ri_0 and Pr) so that a small $|\mathscr{S}t_b/\mathscr{S}h_b|$ ratio is maintained at early stages of flow evolution and before the strain field influence dominates. At lower Reynolds numbers, formation of shear vortices can still be excited on the braid by other instabilities (as will be discussed in the companion paper *MP2*), or other types of vortices such as the SPI-SVBI family might roll up on the braid.

Figure 14(*a,b*) show contour plots similar to figure 12 for the SPI mode with $d = 7$ and at $t = 89$. The SPI is entirely driven by the strain field with the shearing term ($\mathscr{S}h_b$) making a negative contribution. Therefore, a vorticity layer subjected to a pure strain field can accommodate a family of three-dimensional instabilities at the stagnation point which exist over a much broader range of spanwise wavelengths compared with the shear instability. Moreover, the shear acts so as to suppress the strain field-induced instability while the strain field acts so as to suppress the shear modes. Contributions from $\mathscr{H}$ and $\mathscr{D}$ to growth rate of SPI are also very small similar to the SSI. A necessary condition for the SPI to exist is to have $\mathscr{S}t_b > \mathscr{S}h_b$.

To extend discussions of figure 9 on the physical origin of SPI, figure 14(*c,d*) show plots of the perturbation kinetic energy eigenfunction and the perturbation velocity field (overlain on the vorticity contours of the background KH wave), respectively. They show that the onset of the SPI is indeed triggered by interaction of the core's outermost negative vorticity (blue) band and the braid at the stagnation point. This allows for formation of two stagnation points at the tips of the cores' blue vorticity bands. As figure 14(*d*) shows, this interaction leads to splitting into two of the braid stagnation point (in agreement with earlier discussion of the $t = 82$ time frame and the
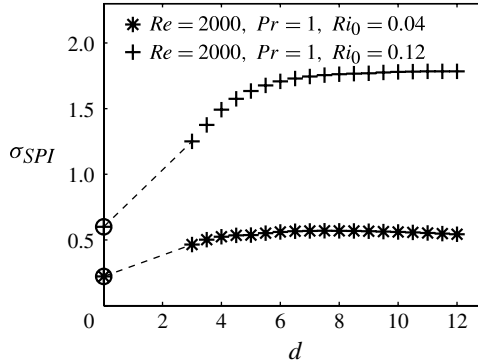
FIGURE 13. Growth rate versus spanwise wavenumber curves for two cases at a $Re = 2000$. Both cases include $d = 0$ data points (encircled) and suggest that the growth rate curves should extend to $d = 0$ in principle.

schematic in figure 9) and allows for formation of a recirculating region which grows by extracting energy from the strain field.

It is important to note that the SPI should not be confused with the so-called hyperbolic instability. The classical hyperbolic instability is that which is responsible for the occurrence of the 'rib-vortices' that develop in unstratifed parallel shear flow and which are precursory in such flows to transition. Very detailed analysis of this instability have been published in the previous literature on non-separable instability analysis (see Smyth & Peltier 1994, Potylitsin & Peltier 1998 and *CP00* for details). The rib vortices generated by classical hyperbolic instability are extensive structures that develop between adjacent vortex cores rather than being isolated initially to the hyperbolic fixed point which is the case for what we are referring to as the SPI. Furthermore, although the classical hyperbolic instability is intrinsically three dimensional, this is not the case for the SPI that occurs in stratified flow. The SPI exists over a range of spanwise wavenumbers that includes $d = 0$ (i.e. in which case it is a two-dimensional mode). However, it is difficult for our methodology to determine growth rates for SPI modes with small spanwise wavenumbers, as the top of the list of unstable modes found by our non-separable stability analysis becomes overly crowded with large families of pairing, SSI and SCI modes (as shown in figure 6e). Therefore, detection of SPI as d tends to zero becomes overly cumbersome. However, in principle, we could complete the SPI curve all of the way to $d = 0$ by increasing the resolution greatly and checking the list of eigenmodes all the way down to number 20 or so.

To verify that the SPI curves in figure 8 should extend all of the way to zero, we set d to be exactly equal to zero in our analysis. This eliminates all SCI modes, as well as many SSI modes and pairing modes and substantially 'cleans up' the spectrum and allows the weakly growing SPI mode to rise further up the list of unstable structures. Figure 13 shows the growth rate curve for SPI for two different cases at higher Reynolds number of 2000 (we consider higher Re as it is easier to detect SPI at $d = 0$ at higher Re; these two cases will be discussed in detail in *MP2*) plotted against d. The figure explicitly includes the case $d = 0$ and unambiguously demonstrates that for both values of the initial Richardson number the growth rate for the two-dimensional version of the SPI mode is simply an extension of the growth rate curve for three-dimensional modes to the $d = 0$ limit.
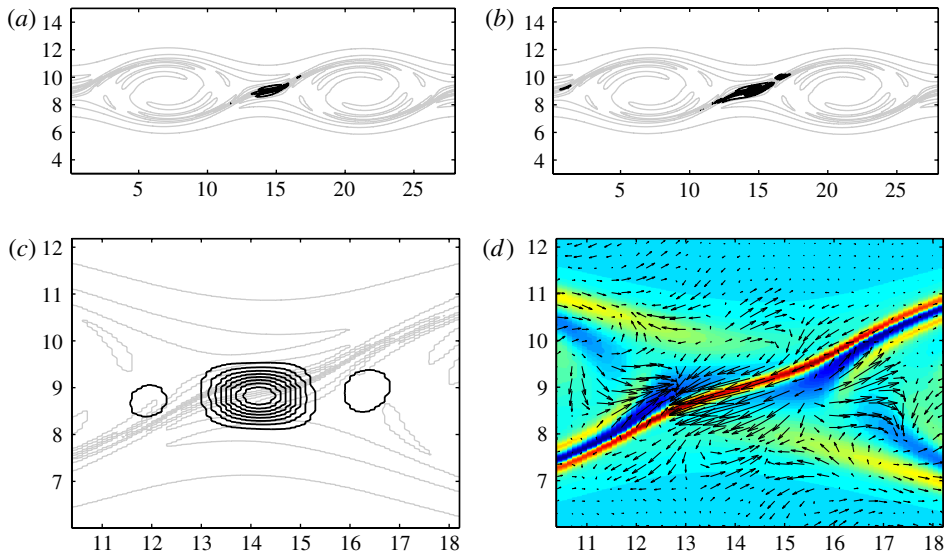
FIGURE 14. Contours of (*a*) $\text{Shear}_{eig}^{braid}$ contour for SPI at $t = 89$, $\sigma_r = 0.8$, $\mathscr{S}h_b = -0.16$, $\mathscr{S}t_b = -0.9$, (*b*) $\text{Strain}_{eig}^{braid}$ contour for SPI at $t = 89$, $\sigma_r = 0.8$, $\mathscr{S}h_b = -0.16$, $\mathscr{S}t_b = -0.9$ and (*c*) perturbation kinetic energy for the SPI at $t = 82$; (*d*) the perturbation velocity field overlain on the vorticity contour of the background KH wave.

At this point it is necessary to discuss the interpretation of the results presented in Dritschel *et al.* (1991) who analysed the stability against two-dimensional perturbations of a tilted two-dimensional unstratified inviscid vorticity layer subjected to a pure strain field. We believe that the unstable modes revealed by their analyses were of stagnation point type rather than the 'conventional Rayleigh shear instability' as referred to in that study. Their analyses reveal a phase-locked mode growing at the stagnation point. The finite amplitude form of that mode corresponds to roll-up of a vortex at the stagnation point with the braid streamwise wavelength of the mode increasing and its growth rate decreasing due to the strain field. To provide convincing evidence for this interpretation, figure 15 shows evolution of the SPI mode at the stagnation point for two different cases. Comparison of this figure with figure 17 of Dritschel *et al.* (1991) reveals clear similarity: namely a change in slope of a segment of the braid at the stagnation point followed by roll up of the segment into an isolated vortex at the stagnation point. There are also differences between the plots of figures 15 and 17 of Dritschel *et al.* (1991) in that in our cases the instability interacts with the growing and approaching vorticity bands inside the primary KH vortex cores. Nevertheless, we expect that the two instabilities are plausibly the same.

Differentiation between the shear instability mode and the SPI on a vorticity filament (such as the braid) is critical for several important reasons. First, our stability analyses demonstrate that the origins of the two instabilities are distinctly different (one extracting its energy from the strain field and the other from the velocity shear) and a great difference in the range of spanwise wavenumbers over which they exist (SSI being a long-wave semi-two-dimensional mode while the SPI is highly three-dimensional and exists over a broad range with a high wavenumber for its fastest growing mode). Moreover, confusion regarding the origins of the two modes can be misleading in interpretation of numerical simulation results. It needs to be pointed out
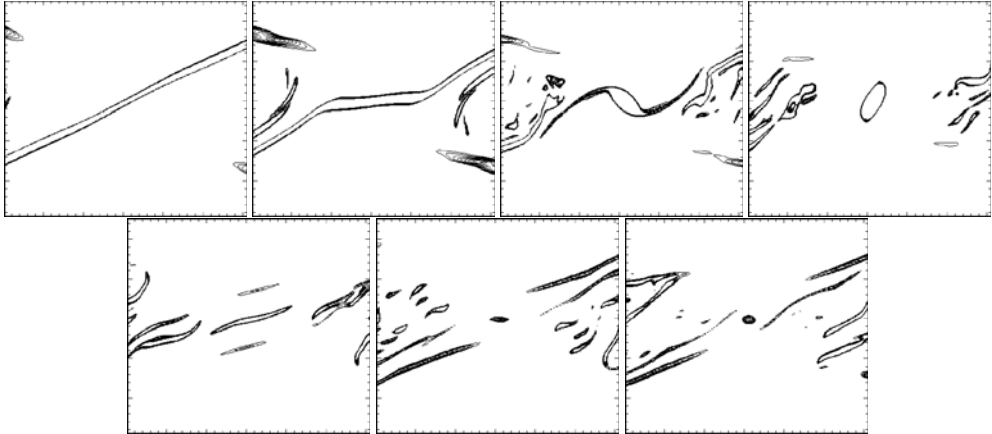
$Pr = 2$, $Ri_0 = 0.12$, $Re = 2000$, $60 < t < 70$
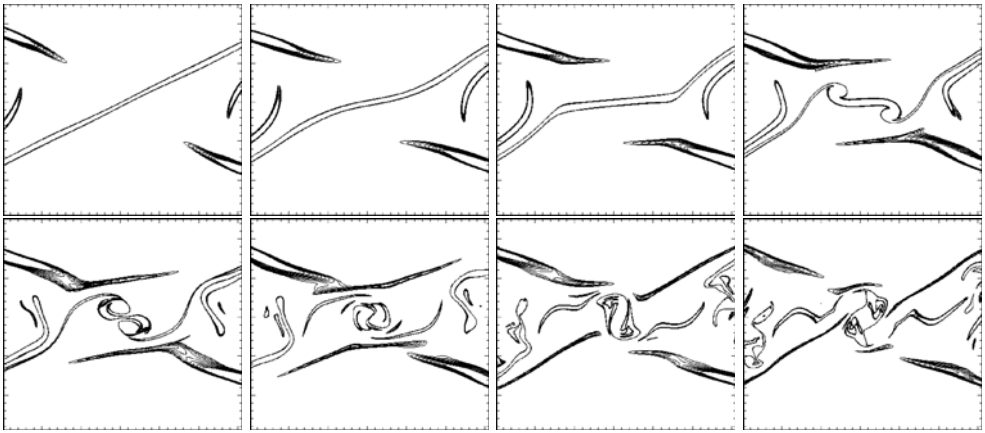
$Pr = 2$, $Ri_0 = 0.12$, $Re = 4000$, $68 < t < 78$

FIGURE 15. Evolution of the SPI is shown by plots (based on the results of two-dimensional simulations) of vorticity contours at the stagnation point for two different cases. Contour plots include 10 levels between $+0.5$ and $+1.5$.

that observational similarities can exist between finite amplitude SPI at low *Re* and a shear-induced vortex formed on the braid in contour plots based on two-dimensional simulation, Staquet (1995) appears to have incorporated several SPI vortices in her analyses of the parameter regime in which SSI may emerge. A complete energetics analyses of the braid vortices and recognition of the difference in phase speed of the SSI and SPI vortices (with SPI being phase locked) aids significantly in distinguishing between the two modes even in the results of two-dimensional simulations.

The stagnation point criterion proposed by Dritschel *et al.* (1991), however, is relevant to the possibility of occurrence of SPI in a two-dimensional flow. Our numerical simulations reveal emergence of SPI on the braid for $\gamma/\Omega < 0.1$ for $Pr = 1$ which is close to the value of 0.065 proposed by Dritschel *et al.* (1991) for an inviscid unstratified vorticity layer. One can construct approximate maps of γ/Ω at the stagnation point for various values of the Prandtl number by employing the
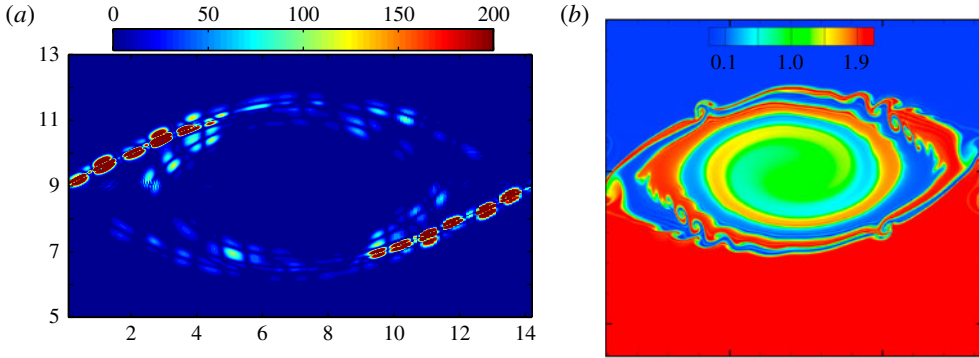
FIGURE 16. (*a*) Perturbation kinetic energy of the SSI mode for case *c*1-1000-0.12 for $t = 73$; (*b*) density contour plot for a case with $Pr = 12$, $Re = 6000$ and $Ri_0 = 0.12$.

quadratic $\gamma - Ri_0$ relation employed in figure 5(*e*) along with the expression

$$\Omega = -\left(\frac{2}{\pi}\right)^{1/2} \frac{Re^{1/2} Ri_0 \sin \psi \, \Delta \rho_b \, Pr^{\beta - 1/2}}{\gamma_s^{1/2}}, \tag{4.32}$$

proposed by *S03* for maximum braid vorticity ($\beta = 0.63$ for $1 < Pr < 7$). One such map for $Pr = 1$ was provided in figure 5(*f*). As SPI is a highly three-dimensional mode, we postpone the investigation of its finite amplitude growth to further study which will involve three-dimensional simulations. Two-dimensional results such as those shown in figure 15 should be treated with caution.

Finally, we point out that the SSI eigenfunction revealed in our analyses in not limited to the braid. As figure 16(*a*) shows, the entire length of the initial vorticity layer at time $t = 0$ (including the parts rolled-up in the cores and the part connecting the cores, i.e. the braid) remains susceptible to shear instability with the wavelength of the unstable mode being proportional to the reduced thickness of the vorticity layer. For low-Reynolds-number and low-Prandtl-number flows, the braid accommodates almost all of the perturbation kinetic energy of the SSI mode as shown in (*a*) of the figure and also in figures 12 and 14. However, at sufficiently large Re and Pr values, the thinning of the vorticity bands inside the cores during the roll-up process increases the gradients across them and overcomes the efficient diffusion inside the cores in such a way that the effective Richardson number of the layers inside the cores becomes subcritical (whatever the critical value might be) and shear instability can grow. To confirm this, we have performed a two-dimensional simulation at $Pr = 12$ and $Re = 6000$ and for $Ri_0 = 0.12$. A density contour plot for this case is shown in figure 16(*b*). For this case, shear instability appears earlier and with greater intensity on the vorticity layers at the periphery and interior of the cores (compared with that of the braid). It is important to note that the shear unstable regions inside the core form at the top and bottom boundary of the convectively unstable regions therefore allowing the possibility of excitation of overturning of those regions at the same time (i.e. emergence of the SCI). For this case, the SPI is the first instability to emerge on the braid and is responsible for formation of several shear vortices on the braid. This extended SSI mode may partially explain the observation of well-mixed core interiors in salt stratified estuarine shear flows as reported in Geyer *et al.* (2010). It is possible that at very high Reynolds number (the value of which will critically depend on both Pr and Ri_0), shear vortices can form on the braid as the primary KH wave rolls up.
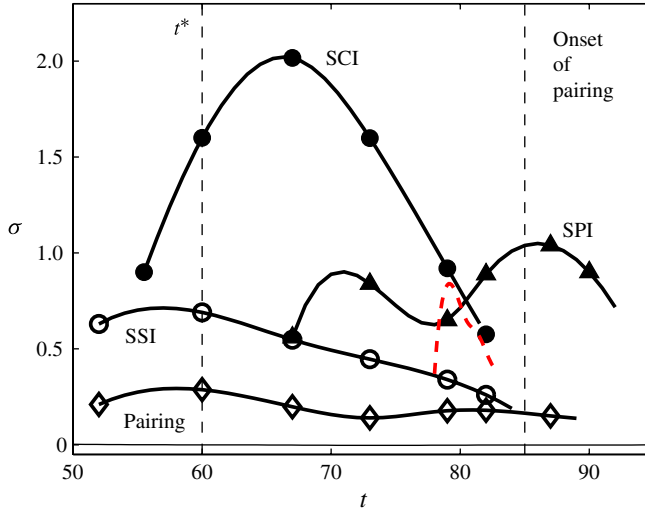
FIGURE 17. (Colour online) The results of the stability analysis for the fastest growing modes of various modes during the evolution of case $c1$-1000-0.12: The solid curve with filled circles for SCI with $d = 8.5$, the solid line with open circles for SSI with $d = 0$, the solid line with diamonds for the pairing instability, the solid line with filled triangles for SPI with $d = 7$, the dashed curve with no marker for the SVBI with $d = 0$, and the thin solid line (almost coincident with the $\sigma = 0$ axis) for the growth rate of the background KH wave, σ_{KH}. The symbols show the actual data points for which the analysis has been done while the lines are spline fits. The vertical dashed line shows the time of maximum $\mathscr{K}'$, t^*.

It will be interesting to investigate whether in those circumstances SSI will be capable of facilitating a rapid and early transition to turbulence eliminating any chance of emergence for the three-dimensional instabilities we have found to be dominant in the $Re < 10^4$ regime. The extension of the braid shear instability to vorticity bands inside the cores has already been reported in Fontane & Joly (2008) for KH waves growing on the interface between two fluids. However, our analyses reveal their existence in the context of stratified shear layers and show that in the regime of very large Pr and Re, the braid in a KH billow formed in a stratified layer tends to act in a way that is similar to an interface between two fluids.

5. Discussion and conclusions

Figure 17 plots the growth rate of the fastest growing modes of the set of secondary instabilities we have identified for the case $c1$-1000-0.12. These growth rates must be compared with that of the time scale of evolution of the background KH wave to verify the validity of our assumption of the existence of a separation of time scales between the secondary instabilities and the basic state wave. The growth rate of the primary KH billow (obtained from (4.15)) is plotted in figure 17 as a thin solid line which almost coincides with the $\sigma_r = 0$ axis. The curve has a maximum value of 0.017 while the minimum value for the mode with the smallest growth rate (i.e. the pairing mode) is 0.138. This confirms the existence of an appropriate time scale separation.

Figure 17 shows that over almost the entire time period between t^* and the onset of pairing which commences at $t \sim 85$ (in our two-dimensional simulation and not in a full three-dimensional flow field) as shown in the figure by the second vertical dashed line, the SCI dominates the other instabilities by a wide margin. Our earlier analysis

in §3.3 also found the *c*1-1000-0.12 case to be in the zone of dominance of the SCI. Since the onset of the SCI is followed by a fast transition to turbulence, emergence of SCI will most probably partly or entirely suppress the emergence of other secondary modes. It was predicted by our heuristic model that the SSI becomes stronger as Re and Ri_0 increase while the probability of SCI occurrence decreases with increase in Ri_0. We will investigate these predictions further in *MP2*. It will be interesting to explore regions in parameter space where two or more of these instabilities can coexist, or where some may precede the secondary convective instability.

Figure 17 shows a monotonic decrease with time in the growth rate of SSI. This is due to the growing negative influence of the straining contribution of the background flow to the growth of the instability as explained in discussion of the table related to figure 12.

According to figure 17, the SPI is characterized by a non-monotonic behaviour, whereas the SSI mode becomes weaker monotonically and the growth rate of the pairing instability shows long-period fluctuations around a mean. This is because the pairing instability depends only on the large-scale structure of the flow whereas the SSI depends on the braid structure (which changes continuously) and the SPI is sensitive to the flow variations at the stagnation point.

An important point follows by comparing the SCI curve in figure 17 with the Ra^u shown in figure 7(*c*). This comparison demonstrates that Ra^u becomes subcritical at approximately the same time as the growth rate of the SCI mode sharply diminishes. This reinforces the validity of our assumption in the construction of the heuristic model that Ra^u provides an acceptable measure of the probability of occurrence of the secondary convective instability. Comparing the growth rate of the SCI (for $Re = 1000$) to the values reported by *KP85* (for $Re = 300$) reveals considerable increase in growth rates with the Reynolds number. This is in agreement with the predictions of our heuristic model.

The probability maps (figures 4 and 5) produced on the basis of the heuristic model suggested that there should exist a wide range in this parameter space in which both braid shear and core convective instabilities may exist in principle. Increase in Re promotes both instabilities while increase in Ri_0 promotes braid shear instability and acts against the probability of occurrence of convective instability. Increase in Pr on the other hand acts in favour of the secondary convective instability and to suppresses the braid shear instability. The Prandtl number influence has important implications for oceanic shear flows and will warrant further investigation.

Since most of the simulations in the published literature devoted to studying the secondary instability of the braid have been restricted to two space dimensions, we questioned the extent to which the results of those studies are relevant to three-dimensional reality. Figure 17 in particular reveals the existence of a number of highly three-dimensional instabilities some or all of which will almost certainly coexist with (if not precede) the two-dimensional instabilities which have been discussed in the two-dimensional simulation-based literature. Therefore, the relevance of such studies to the evolution of a three-dimensional flow, especially in the post-transition phase, is questionable.

We compared the probability map for occurrence of the secondary braid shear instability with the results of our two-dimensional simulations for a wide range of Reynolds and Richardson numbers and for unit Prandtl number. We identified a gap between the supercritical region in the *Re–Ri* space in which SSI might occur (based on the braid Richardson number) and the actual region in which secondary vortices form on the braid in our two-dimensional simulations. This gap exists due to the stabilizing influence of the strain field induced by the vortex cores on the

braid. Our maps of braid Richardson number and γ/Ω show that SSI is likely to emerge for $Ri_B < 0.25$ and $\gamma_s/\Omega_s < 0.1$. We have argued that since the existence of a distinct SPI instability was not recognized in the study of Staquet (1995) due to the two-dimensional nature of the study, it was mistaken for SSI. We have also argued that the shear instability discussed in Dritschel *et al.* (1991) is most probably a SPI which extracts its energy almost entirely from the strain field with the background shear acting so as to suppress it. Confusing the two instabilities may clearly result in misinterpretation of results of numerical simulations. This confusion can be avoided by detailed analysis of the energetics of the structures forming on the braid or by comparing the spanwise wavenumbers of the two instabilities (which is only relevant in the case of a three-dimensional flow). We have further shown that discussion of braid shear instability should not be focused solely on the stagnation point as the SSI eigenfunction extends along the braid. The SSI eigenfunction has a larger spatial extension at early stages of flow evolution and shrinks with time due to evolution of the vortex cores. Therefore, the probability of occurrence of SSI on the braid is very time dependant and greatly diminishes at later stages of flow evolution due to emergence of other three-dimensional secondary instabilities. In *MP2* we show that as the Reynolds number increases, SSI will have a larger growth rate (compared with other instabilities) earlier in flow evolution as its eigenfunction extends for greater distance along the braid and, hence, has a better chance of emerging. Such a conclusion would not be warranted based upon arguments only in terms of Ri_B and γ_s/Ω_s.

Our analyses demonstrated the possibility of emergence of three-dimensional SSI modes with wavelengths comparable to that of the main KH wave. The pairing instability was found to be of a three-dimensional nature in stratified layers in agreement with similar previously reported results for homogeneous shear flows.

Perhaps one of the most important findings of this work, however, concerns the discovery of the existence of the SPI and SVBI modes which develop in the middle of the braid and tend to roll-up or to deform the braid at its stagnation point. These modes exist for a wide range of spanwise wavenumbers. The fastest growing mode of the SPI has a spanwise wavenumber close to that of the fastest growing mode of the secondary convective instability. A observational example of the SPI mode seems to be seen in figure 14 of Moum *et al.* (2003) which shows a KH billow forming on the interface of an internal solitary wave approaching the shore. It may well be that the onset of SPI along with SCI (and other three-dimensional short-wave modes which exist in the high-Reynolds-number regime) is responsible for strongly inhibiting the occurrence of pairing and, thus, the upscale cascade of energy in turbulent stratified shear flows. The possibility of finite amplitude growth of a highly three-dimensional instability which grows at the stagnation point of a strain field in the presence of shear and which extracts its energy from the stain field, may have important implications for turbulence transition in other examples of geophysical flows and calls for further investigation.

It should be noted that even though SPI is hard to distinguish from SSI vortices on the braid in two-dimensional simulations (such as in figure 18 and in simulations of Staquet (1995)), the two have very different spanwise length scales (with SPI being a short-wave mode which will contribute more effectively to transition to turbulence). Moreover, SPI is a phase-locked instability which remains at the stagnation point for a considerable length of time whereas SSI vortices move along the braid and towards the cores upon formation. These two major differences provide a means of exactly distinguishing SPI from SSI in both three-dimensional simulations and in laboratory
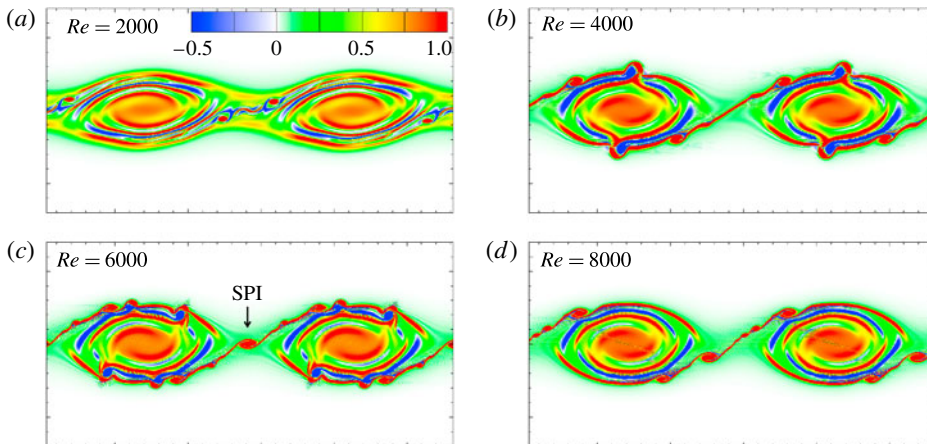
FIGURE 18. Vorticity contours showing braid instabilities for: (*a*) *Re* = 2000; (*b*) *Re* = 4000; (*c*) *Re* = 6000; and (*d*) *Re* = 8000. All four cases correspond to a Richardson number value of 0.12 and a Prandtl number of 1.

experiments (provided that flow conditions required for SPI to grow can be provided in a laboratory setting).

Insofar as the evolution of the SSI is concerned, we have shown (using both the heuristic model and the stability analysis) that an increase in the Reynolds number enhances the probability of occurrence of the SSI. To illustrate this, we plot the vorticity contours for four cases with Reynolds numbers ranging from 2000 to 8000 in figure 18 (note that these contours are obtained from two-dimensional simulations; three-dimensional evolution of the secondary modes discussed herein will be pursued in future work). For this case, the SSI does not grow into a train of small billows as one would expect from the eigenfunctions shown in figure 8. The formation of the two vortices on the braid are triggered by the braid deformation induced by the SVBI. Vortices formed on the braid in figure 18(*b*) (for *Re* = 4000) are of shear type and their emergence has triggered a form of braid deformation which will be discussed in *MP2*. For the *Re* = 6000 case, the first instability to emerge is the SPI which excites formation of numerous secondary shear vortices on the braid. Advection of these vortices to the periphery of the cores by the braid leads to significant deformations in the vortex cores. For figure 18(*d*), the Reynolds number is high enough (8000) that the SSI begins to show characteristics more in harmony with the eigenfunction shown in figure 8. This is because, in agreement with our theoretical predictions, as the Reynolds number increases, the SSI will have a greater probability of emergence at earlier stages of flow evolution and prior to the onset of other modes of instability.

According to our heuristic model, the stratification level is of first-order importance in the competition between the SSI and SCI (and possibly other) modes. Therefore, as the next step of this sleuthing of the inhabitants of the secondary instability zoo it will be important to investigate the effect of variations in the Richardson number on the time evolution of the possibility of occurrence of various modes of instability. This is our main focus in the companion paper *MP2*.

Acknowledgements

Supplementary data

Supplementary data are available at journals.cambridge.org/flm.

Appendix

Figure 19 gives a lexicon of various secondary instabilities discussed in this paper and in *MP2* and table 2 is a summary of acronyms used to refer to previous studies.
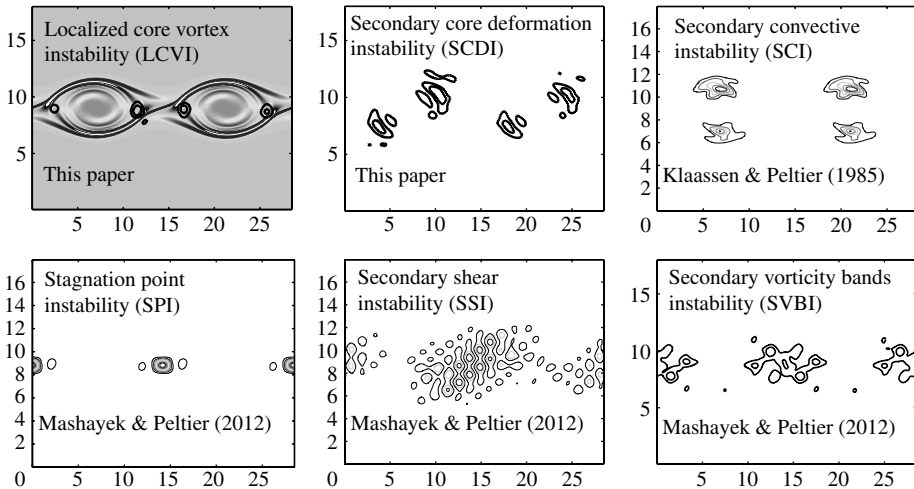

FIGURE 19. Lexicon of various secondary instabilities discussed in this paper and in *MP2*. Each frame contains the reference to the original study which provides details of its corresponding instability. The first frame also shows the underlying background KH billow.

MP2	Mashayek & Peltier (2012)
CS76	Corcos & Sherman (1976)
S03	Smyth (2003)
CP00	Caulfield & Peltier (2000)
KP85	Klaassen & Peltier (1985)
KP89	Klaassen & Peltier (1989)

TABLE 2. Summary of acronyms used to refer to previous studies.

REFERENCES

ASHURST, W. T. & MEIBURG, E. 1988 Three-dimensional shear layers via vortex dynamics. *J. Fluid Mech.* **189**, 87–116.

BEWLEY, T. R. 2012 *Numerical Renaissance: Simulation, Optimization, & Control*. http://renaissance.ucsd.edu/.

BROWNING, K. A. 1971 Structure of the atmosphere in the vicinity of large-amplitude Kelvin–Helmholtz billows. *Q. J. R. Meteorol. Soc.* **97**, 283–299.

BROWNING, K. A. & WATKINS, C. D. 1970 Observations of clear air turbulence by high-power radar. *Nature* **227**, 260–263.

CAULFIELD, C. P. & PELTIER, W. R. 1994 Three-dimensionalization of the stratified mixing layer. *Phys. Fluids* **6**, 3803–3805.

CAULFIELD, C. & PELTIER, W. R. 2000 Anatomy of the mixing transition in homogeneous and stratified free shear layers. *J. Fluid Mech.* **413**, 1–47.

CAULFIELD, C. P., YOSHIDA, S. & PELTIER, W. R. 1996 Secondary instability and three-dimensionalization in a laboratory accelerating shear layer. *Dyn. Atmos. Oceans* **23**, 125–138.

CLEVER, R. M. & BUSSE, F. H. 1974 Transition to time-dependant convection. *J. Fluid Mech.* **65**, 625–645.

CORCOS, G. & SHERMAN, F. 1976 Vorticity concentration and the dynamics of unstable free shear layers. *J. Fluid Mech.* **73**, 241–264.

CORTESI, A. B., YADIGAROGLU, G. & BANNERJEE, S. 1998 Numerical investigation of the formation of three-dimensional structures in stably stratified mixing layers. *Phys. Fluids* **10**, 1449–1473.

DAVIS, P. A. & PELTIER, W. R. 1979 Some characteristics of the Kelvin Helmholtz and resonant over-reflection modes of shear flow instability and of their interaction through vortex pairing. *J. Atmos. Sci.* **36**, 2394–2412.

DRAZIN, P. G. & REID, W. H. 1981 *Hydrodynamic Stability*. Cambridge University Press.

DRITSCHEL, D., HAYNES, P., JUCKES, M. & SHEPHERD, T. 1991 The stability of a two-dimensional vorticity filament under uniform strain. *J. Fluid Mech.* **230**, 647–665.

FONTANE, J. & JOLY, L. 2008 The stability of the variable-density Kelvin–Helmholtz billow. *J. Fluid Mech.* **612**, 237–260.

GEYER, W. R., LAVERY, A. C., SCULLY, M. E. & TROWBRIDGE, J. H. 2010 Mixing by shear instability at high Reynolds number. *Geophys. Res. Lett.* **37**, L22607.

GOSSARD, E. E. 1990 Radar research on the atmospheric boundary layer. In *Radar in Meteorology* (ed. D. Atlas), pp. 477–527. American Meteorological Society, chap. 27a.

HAREN, H. V. & GOSTIAUX, L. 2010 A deep ocean Kelvin–Helmholtz billow train. *Geophys. Res. Lett.* **37**, L03605.

HAURY, L. R., BRISCOE, M. G. & ORR, M. H. 1979 Tidally generated internal wave packets in massachusetts bay. *Nature* **278**, 312–317.

HAZEL, P. 1972 Numerical studies of the stability of inviscid parallel shear flows. *J. Fluid Mech.* **51**, 39–62.

HOLT, J. T. 1988 Experiments on Kelvin–Helmholtz billows influenced by boundaries. *Geophys. Astrophys. Fluid Dyn.* **89**, 205–233.

HOWARD, L. N. 1961 Note on a paper of John W. Miles. *J. Fluid Mech.* **10**, 509–512.

JORDAN, D. W. & SMITH, P. 1977 *Nonlinear Ordinary Differential Equations*. Oxford University Press.

KELVIN, LORD 1871 Hydrokinetic solutions and observations. *Phil. Mag.* **10**, 155–168.

KLAASSEN, G. P. & PELTIER, W. R. 1985 The onset of turbulence in finite amplitude Kelvin–Helmholtz billows. *J. Fluid Mech.* **155**, 1–35.

KLAASSEN, G. P. & PELTIER, W. R. 1989 The role of transverse secondary instabilities in the evolution of free shear layers. *J. Fluid Mech.* **202**, 367–402.

KLAASSEN, G. P. & PELTIER, W. R. 1991 The influence of stratification on secondary instabilities in free shear layers. *J. Fluid Mech.* **227**, 71–106.

LAMB, G. & FARMER, D. 2011 Instabilities in an internal solitary-like wave on the oregon shelf. *J. Phys. Oceanogr.* **41**, 67–87.

LUCE, H., MEGA, T., YAMAMOTO, M. K., YAMAMOTO, M., HASHIGUCHI, H., FUKAO, S., NISHI,N., TAJIRI, T. & NAKAZATO, M. 2010 Observations of Kelvin–Helmholtz instability at a cloud base with the middle and upper atmosphere (MU) and weather radars. *J. Geophys. Res.* **115**, D19116.

LUDLAM, F. H. 1967 Characteristics of billow clouds and their relation to clear-air turbulence. *Q. J. R. Meteorol. Soc.* **93**, 419–435.

MARMORINO, G. O. 1987 Observations of small scale mixing processes in the seasonal thermocline. Part ii. Wave breaking. *J. Phys. Oceanogr.* **17**, 1348–1355.

MASHAYEK, A. & PELTIER, W. R. 2012 The 'zoo' of secondary instabilities precursory to stratified shear flow transition. Part 2 The influence of stratification. *J. Fluid Mech.* **708**, 45–70.

MILES, J. W. 1961 On the stability of heterogeneous shear flows. *J. Fluid Mech.* **10**, 496–508.

MOUM, J. N., FARMER, D. M., SMITH, W. D., ARMI, L. & VAGLE, S. 2003 Structure and generation of turbulence at interfaces strained by internal solitary waves propagating shoreward over the continental shelf. *J. Phys. Oceanogr.* **33**, 2093–2112.

PELTIER, W. R. & CAULFIELD, C. 2003 Mixing efficiency in stratified shear flows. *Annu. Rev. Fluid Mech.* **35**, 135–167.

PIERREHUMBERT, R. T. & WIDNALL, S. E. 1982 The two- and three-dimensional instabilities of a spatially periodic shear layer. *J. Fluid Mech.* **114**, 59–82.

POTYLITSIN, P. & PELTIER, W. R. 1998 Stratification effects on the stability of columnar vortices on the f-plane. *J. Fluid Mech.* **355**, 45–79.

RUELLE, D. & TAKENS, F. 1971 On the nature of turbulence. *Commun. Math. Phys.* **20**, 167–192.

SMYTH, W. D. 2003 Secondary Kelvin–Helmholtz instability in weakly stratified shear flow. *J. Fluid Mech.* **497**, 67–98.

SMYTH, W. D., MOUM, J. & CALDWELL, D. 2001 The efficiency of mixing in turbulent patches: inferences from direct simulations and microstructure observations. *J. Phys. Oceanogr.* **31**, 1969–1992.

SMYTH, W. D. & PELTIER, W. R. 1990 Three-dimensional primary instabilities of a stratified, dissipative, parallel flow. *Geophys. Astrophys. Fluid Dyn.* **52**, 249–261.

SMYTH, W. D. & PELTIER, W. R. 1991 Instability and transition in finite amplitude Kelvin–Helmholtz and Holmboe waves. *J. Fluid Mech.* **228**, 387–415.

SMYTH, W. D. & PELTIER, W. R. 1993 Two-dimensional turbulence in homogeneous and stratified shear layers. *Geophys. Astrophys. Fluid Dyn.* **69**, 1–32.

SMYTH, W. D. & PELTIER, W. R. 1994 Three-dimensionalization of barotropic vortices on the f-plane. *J. Fluid Mech.* **265**, 25–64.

STAQUET, C. 1995 Two-dimensional secondary instabilities in a strongly stratified shear layer. *J. Fluid Mech.* **296**, 73–126.

STAQUET, C. 2000 Mixing in a stably stratified shear layer: two- and three-dimensional numerical experiments. *Fluid. Dyn. Res.* **27**, 367–404.

STUART, T. 1967 On finite amplitude oscillations in laminar mixing layers. *J. Fluid Mech.* **29**, 417–440.

TAYLOR, J. R. 2007 Numerical simulations of the stratified oceanic bottom layer. PhD thesis, University of California, San Diego.

THORPE, S. A. 1971 Experiments on the instability of stratified shear flows: miscible fluids. *J. Fluid Mech.* **46**, 299–319.

THORPE, S. A. 1978 The near-surface ocean mixing layer in stable heating conditions. *J. Geophys. Res.* **83**, 2875–2885.

THORPE, S. A. 1981 An experimental study of critical layers. *J. Fluid Mech.* **103**, 321–344.

THORPE, S. A. 1985 Small-scale processes in the upper ocean boundary layer. *Nature* **318**, 519–522.

THORPE, S. A. 1987 Transitional phenomena and the development of turbulence in stratified fluids: a review. *J. Geophys. Res.* **92**, 5231–5248.

THORPE, S. A. 2005 *The Turbulent Ocean*. Cambridge University Press.

WINANT, D. & BROWAND, K. 1974 Vortex pairing: the mechanism of turbulent mixing layer growth at moderate Reynolds numbers. *J. Fluid Mech.* **63**, 237–255.

WOODS, J. D. 1968 Wave induced shear instability in the summer thermocline. *J. Fluid Mech.* **32**, 791–800.